

1                   **Fluid evolution in the Strange Lake granitic pluton, Canada:**  
2                   **Implications for HFSE mobilisation**

3   <sup>1\*</sup>O.V. Vasyukova, <sup>1</sup>A.E. Williams-Jones and <sup>2</sup>N.J.F. Blamey  
4   <sup>1</sup>Department of Earth and Planetary Sciences, McGill University, 3450 University Street  
5   Montreal, Quebec, Canada, H3A 0E8.  
  
6   <sup>2</sup>Department of Earth Sciences, Brock University, 1812 Sir Isaac Brock Way, St. Catherines,  
7   Ontario, Canada, L2S 3A1  
8  
9   \*corresponding author, [olga.vasyukova@mcgill.ca](mailto:olga.vasyukova@mcgill.ca)

10   **Abstract**

11   Strange Lake is a mid-Proterozoic peralkaline granite pluton (Québec-Labrador, Canada) that  
12   underwent extreme enrichment in high field strength elements (HFSE), including the rare earth  
13   elements (REE). The HFSE mineralisation is confined to highly altered pegmatites and the most  
14   altered parts of the granites, implying a genetic association between hydrothermal fluids and  
15   HFSE enrichment. This study uses analyses of fluid inclusions to investigate the hydrothermal  
16   evolution of the Strange Lake pluton and the role of hydrothermal processes in concentrating the  
17   HFSE to potentially exploitable levels.  
  
18   Five groups of inclusions were distinguished. From earliest to latest, these groups are: primary  
19   aqueous inclusions (~25 wt.% NaCl eq.) associated with melt inclusions (Group 1); primary

aqueous inclusions (13-23 wt.% NaCl eq.) associated with CH<sub>4</sub> inclusions (Groups 2a and b); primary aqueous inclusions (~9 wt.% NaCl eq.) associated with CO<sub>2</sub> inclusions (Group 3); primary aqueous inclusions (~9 wt.% NaCl eq.), which contain no carbonic component (Group 4); and finally, secondary aqueous inclusions (19 wt.% NaCl eq.), including inclusions that outline mineral pseudomorphs, also with no detectable carbonic component (Group 5). Most of the inclusions (except those in Group 5) have conspicuous 'implosion' haloes, evident as numerous tiny voids. This indicates that the inclusions re-equilibrated, most likely during isobaric cooling.

Fluid evolution commenced with the exsolution of a saline aqueous liquid (~25 wt.% NaCl eq.) and an immiscible CH<sub>4</sub>+H<sub>2</sub> gas from the pegmatitic melt at temperatures of ~450-500 °C and a pressure of ~1100 bars. During isobaric cooling, the gas component of the fluid was gradually oxidised, evolving from being CH<sub>4</sub>-dominant to a CH<sub>4</sub> fluid with a significant proportion of higher order hydrocarbons (due to oxidative coupling of methane induced by the consumption of O<sub>2</sub> through the alteration of arfvedsonite to aegirine; ~325-360°C), and finally to a CO<sub>2</sub>-dominated fluid at ~300 °C. The apparent salinity of the aqueous fluid decreased from ~25 to ~4.5 wt.% NaCl eq. due to fluid-rock interaction. The latter also caused precipitation of nahcolite (as a result of the reaction of newly formed CO<sub>2</sub> with sodium from decomposing minerals), formation of pseudomorphs after primary Na-zirconosilicates and Na-titanosilicates and replacement of primary REE-silicates by bastnäsite-(Ce). Owing to this interaction, the carbonic component of the fluid was consumed which, together with the consumption of H<sub>2</sub>O to form Al-, K- and Fe-phyllsilicates, contributed to an increase in the fluid salinity (up to ~19 wt.% NaCl eq.).

Light rare earth elements (LREE) were remobilised over 10s to 100s of metres by the high temperature high salinity fluid (preserved as Group 1 and 2a inclusions), whereas heavy rare earth elements (HREE) were remobilised on a much smaller scale by a late, low temperature high salinity fluid (trapped as inclusion Group 5). Fluid preserved as inclusion Group 3 may have been responsible for remobilisation of Zr and Ti.

## **Introduction**

The evolution of fluids exsolving from anorogenic granites is of particular interest because such granites are commonly enriched in a variety of high field strength elements, including the rare earth elements, in some cases to exploitable levels, and because these fluids may play an important role in the concentration process. One such granite is Strange Lake, which is currently the target of exploration and where a resource comprising 278 Mt grading 0.93 wt.% total rare earth element oxides (of which 39 % are HREE), 1.92 wt.% ZrO<sub>2</sub> and 0.18 wt.% Nb<sub>2</sub>O<sub>5</sub>, has been discovered ([www.questrareminerals.com](http://www.questrareminerals.com)) in late-formed pegmatites (B-Zone, see below).

Although much of the concentration of the ore metals at Strange Lake was due to magmatic processes, i.e., fractional crystallisation and the separation of an immiscible fluoride melt that preferentially sequestered the REE (Boily and Williams-Jones, 1994; Vasyukova and Williams-Jones, 2014, 2016), hydrothermal processes were important in further concentrating the metals and redistributing them into secondary minerals that are more amenable to beneficiation than their magmatic precursors (Salvi and Williams-Jones, 1996; Gysi and Williams-Jones, 2013).

Previous studies of Strange Lake identified a compositionally diverse array of quartz-hosted fluid inclusion types in both the granites and the pegmatites, including NaCl-rich high temperature and

CaCl<sub>2</sub>-rich low temperature aqueous inclusions and inclusions with a carbonic phase ranging in composition from CH<sub>4</sub> to CO<sub>2</sub>-rich (Salvi and Williams-Jones, 1990, 1992, 1996, 1997, 2006). According to these studies, the first fluids to be trapped were a NaCl-rich aqueous liquid and a CH<sub>4</sub>-rich supercritical fluid (Salvi and Williams-Jones, 1992, 1996). The aqueous liquid was interpreted to have exsolved from the magma at a temperature of 500-600 °C and  $fO_2$  2-3 units below the QFM buffer, and to have been accompanied by a mixture of CO, CO<sub>2</sub> and CH<sub>4</sub> (Salvi and Williams-Jones, 1997, 2006). This liquid is considered to have been responsible for the alteration of arfvedsonite to aegirine, which produced H<sub>2</sub>, and is thought to have transformed the CO and CO<sub>2</sub> into CH<sub>4</sub> and higher hydrocarbons through a magnetite-catalysed Fischer-Tropsch synthesis (Salvi and Williams-Jones, 1997). The subsequent evolution of the system is interpreted to have involved the introduction of a much lower temperature, CaCl<sub>2</sub>-rich aqueous liquid of probable external origin that mixed with the magmatic fluids and oxidised the carbonic phase to CO<sub>2</sub> (Salvi and Williams-Jones, 1990, 1992). The widespread evidence of hematisation, the replacement of Na-bearing titanosilicates and zirconosilicates by Ca-bearing equivalents and the crystallisation of a number of REE minerals were attributed to this fluid (Salvi and Williams-Jones, 2006).

In this paper, we build on the earlier fluid inclusion studies by reporting new data for previously unrecognised fluid inclusion types associated with melt inclusions, adding to the data available for the other types of inclusions and re-interpreting the fluid evolution of the Strange Lake hydrothermal system. Using these data, temperature- $fO_2$  and temperature-pressure paths are reconstructed that describe the evolution of the fluid and fluid-rock interaction, and are

consistent with an alternative explanation to Fischer-Tropsch synthesis for the origin of the higher order hydrocarbons.

## **Geological setting**

The Strange Lake granites are Mesoproterozoic ( $1240 \pm 2$  Ma; Miller et al. (1997) and were emplaced along the contact between an Elsonian quartz monzonite massif and paragneisses of Hudsonian age (Fig. 1). Three main intrusive phases have been distinguished within the complex based on the nature of the alkali feldspars. Hypersolvus granite was the earliest and least evolved. It occupies the central part of the pluton, and is characterized by the presence of perthite and an absence of primary albite (Nassif, 1993). Subsolvus granite is the most evolved, volumetrically the most abundant, and occupies the outer part of the pluton. This granite contains discrete primary microcline and albite crystals. The third granitic phase, transsolvus granite, contains perthite as a phenocryst phase and primary albite and microcline in the groundmass. In addition to feldspar and quartz, the three granite facies also contain arfvedsonite as a major rock-forming mineral and a number of 'exotic' minerals containing high concentrations of high field strength elements (HFSE). The concentration of the HFSE increases from the hypersolvus to the subsolvus granite.

Swarms of pegmatites are observed in two localities, namely in the north-west (B-Zone) and the central part (Main-zone) of the pluton (Fig. 1), where they form sets of subhorizontal lenses up to 20 m thick. The pegmatites are commonly zoned, and are characterized by a marginal facies consisting of quartz, K-feldspar, arfvedsonite and zirconosilicate and titanosilicate minerals, and a core dominated by fluorite and quartz. They are strongly altered and, as noted in the

introduction, host the bulk of the potential economic mineralisation; a REE-Zr-Nb resource was identified in the early 1980s (Zajac et al., 1984), subsequently referred to as the Main-Zone, and a second REE-Zr-Nb resource, the B-Zone in the mid 2000s ([www.questrareminerals.com](http://www.questrareminerals.com)). Hydrothermal fluids mobilised significant amounts of the rare metals, particularly the LREE, into the adjacent granite (Gysi et al., 2016). The rare metal mineralisation comprises a large number of minerals, including allanite-(Ce), armstrongite, bastnäsité-(Ce), elpidite, fluocerite-(Ce), gadolinite-(Y), gagarinite-(Y), gittinsite, kainosite-(Y), monazite-(Ce), pyrochlore, titanite and zircon.

## **Methodology**

### ***Microthermometry***

Microthermometric measurements were made on doubly polished wafers approximately 150 µm thick using a Linkam THMS600 fluid inclusion stage in the Hydrothermal Geochemistry Laboratory at McGill University. The stage was calibrated by measuring the critical and melting temperature of pure water (374.1 and 0 °C, respectively), the critical and melting temperature of pure CO<sub>2</sub> (31.15 and -56.6 °C, respectively), and the initial ice melting temperature (eutectic temperature) of NaCl and KCl aqueous solutions (-21.2 and -10.8 °C, respectively) in synthetic inclusions. The properties of the gas-rich fluid inclusions were determined using the computer software package FLUIDS of Ronald Bakker (2003) (<http://fluids.unileoben.ac.at>); the program BULK was used to calculate the fluid density and the program ISOC the positions of the isochores. Properties of the aqueous inclusions were determined using the on-line computer software package of the Zhenhao Duan Research Group ([6](http://models.kl-</a></p></div><div data-bbox=)

[edi.ac.cn/fluidinc/h2o\\_nacl/calc.php](http://edi.ac.cn/fluidinc/h2o_nacl/calc.php)). The equations of state (EOS) of Bakker (1999) and (Duan et al., 1992a, b, 1996) were used to determine PVT conditions for the gas-rich inclusions.

### ***Bulk gas analyses***

The proportions of the different gas species in the bulk fluid were determined by crushing ~1 g of quartz crystals and analysing the released gas using Pfeiffer Vacuum Prisma quadrupole mass spectrometers at the New Mexico Institute of Mining and Technology as described in Blamey (2012) and Blamey et al. (2015). Samples for the analyses were chosen on the basis of petrography. Each sample was dominated by a single inclusion-group, except for Sample 7, which contained roughly equal proportions of two inclusion groups (Table 1; fluid inclusion groups are defined below). Match head-sized samples were selected, cleaned with nitric acid to remove surface organic material, rinsed several times with deionized water, and then dried at <100 °C for 2-4 h. The samples were crushed incrementally under a vacuum of  $\sim 10^{-8}$  Torr, producing 6 to 10 releases of fluid. The analyses were performed using two Pfeiffer Prisma quadrupole mass spectrometers operating in fast scan peak-hopping mode, and provided data for the following gaseous species: H<sub>2</sub>, He, CH<sub>4</sub>, H<sub>2</sub>O, N<sub>2</sub>, O<sub>2</sub>, H<sub>2</sub>S, Ar, CO<sub>2</sub>, C<sub>2</sub>H<sub>4</sub>, C<sub>2</sub>H<sub>6</sub>, SO<sub>2</sub>, C<sub>3</sub>H<sub>6</sub>, C<sub>3</sub>H<sub>8</sub>, C<sub>4</sub>H<sub>8</sub>, C<sub>4</sub>H<sub>10</sub> and C<sub>6</sub>H<sub>6</sub>. Instrument calibration was performed using commercial gas mixtures, capillary tubes filled with gas mixtures, and three in-house fluid inclusion gas standards (Blamey et al., 2015). Hydrogen was detected reliably when its mass proportion was above about 50 ppm; the detection limit for the other inorganic gas species was about 0.2 ppm. Detection limits for organic species were ~ 2 ppm. Seven capillary tubes with a 1 mbar encapsulated atmosphere were analysed and yielded N<sub>2</sub>/Ar ratios of 83.4 with a standard deviation of 0.4. This compares favourably with the atmospheric N<sub>2</sub>/Ar ratio of 83.6 and

translates to a 0.5% accuracy for artificial inclusions made under laboratory conditions. The precision using natural inclusions for the major gas species, i.e., CO<sub>2</sub>, CH<sub>4</sub> and N<sub>2</sub>, was  $\pm 5\%$ , and for minor species was  $\pm 10\%$ .

### ***Raman spectroscopy***

Raman analyses were performed at McGill University, in the Biointerface Laboratory (<http://biointerfacelab.mcgill.ca/instruments.html>) using a Bruker Senterra confocal Raman microscope equipped with a 532 laser. This enabled analysis of peaks within a wavelength range from 30 to 3700 cm<sup>-1</sup>, and identification of the gases, H<sub>2</sub> (586 cm<sup>-1</sup>, the strongest H<sub>2</sub> peak at 4156 cm<sup>-1</sup> could not be observed due to the restricted wavelength range of the spectrometer), CH<sub>4</sub> (2910-2918 cm<sup>-1</sup>), C<sub>2</sub>H<sub>6</sub> (993 and 2954 cm<sup>-1</sup>), C<sub>3</sub>H<sub>8</sub> (2890 cm<sup>-1</sup>) and CO<sub>2</sub> (1284 and 1387 cm<sup>-1</sup>), and the minerals, nahcolite, albite and microcline (Burke, 2001; Frezzotti et al., 2012). Because the proportions of the gases differed considerably among inclusions, even within a single sample, we did not calibrate the instrument to calculate these proportions. Instead, the average proportions of the different gases in each sample were determined from the mass spectrometric analyses described above.

### ***Thermodynamic calculations***

Thermodynamic calculations of the gas proportions were performed using the software package HCh (Shvarov, 1999; Shvarov and Bastrakov, 1999) and the algorithm employed by Salvi and Williams-Jones (1997). Thermodynamic data for ethane and propane were taken from Stull et al. (1969), Chao et al. (1973) and Stryjek and Vera (1986). Data for the other gases, i.e., H<sub>2</sub>, H<sub>2</sub>O,



CO, CO<sub>2</sub>, CH<sub>4</sub>, were from CODATA (1978), Robie et al (1978), Stryjek and Vera (1986), Reid et al. (1987) and Robie and Hemingway (1995).

## **Results**

### ***Samples***

Sixteen samples that are representative of the different rock-types in the Strange Lake Pluton were selected for detailed fluid inclusion study (Table 1 and Fig. 1). Seven of the samples were taken from two drill holes (ALT12007 and SL-11), one of which is located in the Alterra Zone (Samples 2, 11 and 7) and the other in the B-Zone (Samples SL-11-14, SL-11-22, SL-11-43 and SL-11-45). The remaining six samples are from outcrops, and represent hypersolvus granite (204794), subsolvus granite (204739 and 204741), pegmatite within transsolvus granite (204722 and 16) and pegmatite within hypersolvus granite (4 and 13). Sample 13 and the seven drill core samples are from quartz rich pegmatite cores, whereas Samples 4, 16, and 204722 are from pegmatite border zones (Table 1). Three of the samples are from fresh pegmatite (4, 16 and 204722), whereas the rest are from altered granite and pegmatite (Table 1). Samples 10205 and 204762 are of typical unaltered hypersolvus and subsolvus granite, respectively. All of the samples, except for Sample 7, are dominated by a single group of fluid inclusions (fluid inclusion groups are defined below). Sample 7 contains roughly equal proportions of two fluid inclusion groups, namely Group 4 and Group 5 inclusions; there are also minor proportions of Group 5 fluid inclusions in Samples SL-11-14, SL-11-22 and SL-11-45 (Table 1).

## *Fluid inclusion types and assemblages*

Based on composition, six types of inclusions were distinguished. The principal characteristics of these inclusion types are illustrated and described in Table 2. Detailed information on the microthermometric behaviour of the inclusions that were analysed is given in APPENDIX A. Where possible, these data are reported statistically (mean, standard deviation) for assemblages of inclusions, in which a single fluid inclusion assemblage (FIA) represents a family of inclusions interpreted to have been trapped at the same time, e.g., as shown by their occurrence along the same growth zone or healed fracture (Goldstein, 2001). In many cases, notably for single inclusions, carbonic inclusions or the carbonic phase of aqueous-carbonic inclusions, for which the datasets were very small, data for individual inclusions are reported.

Type I inclusions are interpreted to represent melt inclusions. They are large (20-70  $\mu\text{m}$  in diameter), multi-solid inclusions that contain K-feldspar, Na-K-zirconosilicates, arfvedsonite, astrophyllite, villiaumite and in some cases REE-fluorides or REE-fluorocarbonates (the minerals were identified in opened inclusions using a scanning electron microscope (SEM) equipped with an energy dispersive X-ray spectrometer (EDS).

Type II inclusions are large (up to 50  $\mu\text{m}$  in diameter), dark, comprise one-phase at room temperature and are  $\text{CH}_4$ -dominated. These inclusions also contain  $\text{H}_2$  and/or higher carbon number hydrocarbons, such as  $\text{C}_2\text{H}_6$  and  $\text{C}_3\text{H}_8$ , which will be described in detail below as part of the Group 2b family of inclusions.

Type III inclusions are similar in shape and size to Type II inclusions but are darker. Unlike Type II inclusions, they are either empty or contain only traces of  $\text{CH}_4$  or  $\text{CO}_2$ .

Type IV inclusions are aqueous. Their size varies among samples, and earlier inclusions tend to be smaller (5-10  $\mu\text{m}$  in diameter) than later inclusions (10-20  $\mu\text{m}$  in diameter). The shapes, phase ratios and microthermometric behaviour of these inclusions are described later in the context of the different fluid inclusion groups.

Type V inclusions are large (15-40  $\mu\text{m}$  in diameter) and comprise varying proportions of aqueous and carbonic phases. The composition of the carbonic phase also varies, with the inclusions in some samples being  $\text{CH}_4$ -dominated and in other samples  $\text{CO}_2$ -dominated.

Type VI inclusions are aqueous, solid-bearing and quite variable in size (5-25  $\mu\text{m}$  in diameter). Three subtypes have been distinguished (Table 1): Subtype VI-1, in which the solids are euhedral and comprise either halite or nahcolite; Subtype VI-2, in which anhedral nahcolite crystals form after freezing/heating cycles; and Subtype VI-3 inclusions that contain anhedral crystals of silicate minerals (microcline, albite, zircon and titanite were identified by Raman spectrometry and SEM-EDS analyses in opened inclusions), which were not affected by cooling or heating.

Owing to the compositional complexity of the inclusions and our wish to understand the fluid evolution, we have chosen to classify them and report their microthermometric behaviour and compositions on the basis of their spatial/textural relationships. Five groups of fluid inclusions were distinguished (Table 2). These are:

1. Aqueous inclusions spatially associated with melt inclusions;
2. Spatially associated  $\text{CH}_4$ -rich and aqueous inclusions;

3. Spatially associated CO<sub>2</sub>-rich and aqueous inclusions, including those containing a crystal;
4. Aqueous inclusions with no obvious relationship to gas-rich inclusions;
5. Late inclusions spatially associated with mineral pseudomorphs and other secondary inclusions.

Each of the inclusion groups was trapped at different pressure-temperature conditions (see below). Inclusion distribution, the fluid composition and characteristic textures of each group of inclusions are described in detail in the paragraphs that follow.

#### ***Group 1***

Group 1 comprises aqueous inclusions (Types IV and VI-1, Table 2), aqueous-carbonic inclusions (Type V) and associated melt inclusions (Type I, Table 2). The melt inclusions are either isolated or localised in trails that, in some cases, are parallel to each other (inserts in Fig. 2b and d), and are interpreted to be growth zones. The aqueous inclusions form haloes around the melt inclusions or are located within the same growth zones (Fig. 2a and b). This group occurs in quartz of the border zones of pegmatites (sample 204722, Table 1 and 2). The Type IV aqueous inclusions are small (5-10 µm), round or oval-shaped, but in some cases they display well-developed negative crystal shapes. They contain a small vapour bubble and the liquid/vapour ratio is ~90/10 (Fig. 2a). Some of the aqueous inclusions (Type VI-1) contain a tiny cube (most likely halite) and a vapour bubble of similar size; the proportion of liquid to the other phases is ~80/20 (Fig. 2c). In both Type IV and VI-1 inclusions there is no detectable carbonic gas in the

vapour bubble. Only one confirmed Type V (CH<sub>4</sub>-bearing) inclusion was observed in a Group 1 association. This inclusion is shown in Figure 2b and decrepitated during subsequent heating.

On heating, the ice in frozen Type IV inclusions melts between -22 and -11 °C and where observed, the hydrohalite dissolves between -13.2 and 0 °C. The majority of inclusions, however, undergo most of their melting at ~ -22 °C. If a halite cube is present (Type VI-1 inclusions), it dissolves at ~185 °C (APPENDIX A). The mean salinity of Type IV (and Type VI-1) fluid inclusion assemblages (FIAs) varies between 15.0 and 33.9 wt.% NaCl eq. (Fig. 3, APPENDIX A); the median value is 25 wt.% NaCl eq. (Table 2). Approximately 70-80 % of the aqueous inclusions homogenised by disappearance of the vapour bubble (a few Type VI-1 inclusions homogenised by dissolution of the solid); the remaining 20-30 % of the inclusions decrepitated during heating at ~140-150 °C. There was massive decrepitation at ~180 °C. The mean homogenisation temperature of these inclusions for individual FIAs ranged from at 86 to 134°C (APPENDIX A); the overall mean homogenisation temperature was 110 °C (Table 2).

## ***Group 2***

Group 2 consists of spatially associated carbonic (Type II), aqueous (Type IV) and mixed aqueous-carbonic (Type V) inclusions (Table 2). These inclusions are found in the border zones and cores of unaltered pegmatites (Samples 16, 204722 and 13, Table 1). In most cases, they show a random 3D distribution and are interpreted to be primary (Fig. 4a-c); in a few cases they occur along healed fractures (Fig. 4d). One such fracture crosscutting growth zones containing Group 1 inclusions is illustrated in Figure 2d (sample 204722). Based on the composition of the

aqueous (salinity) and carbonic (higher hydrocarbon content) components as well as the presence of H<sub>2</sub>, two subgroups were distinguished (Table 2).

#### **Subgroup 2a**

Inclusions of Subgroup 2a are common in samples of unaltered border pegmatites (16 and 204722, Tables 1 and 2). The carbonic (Type II) inclusions (Fig. 4a and b) are dark, large (15-40 µm and in rare cases up to 50 µm in diameter), spherical or ellipsoidal, and in some cases have well-developed faces (negative crystals). They are composed mainly of CH<sub>4</sub> but contain appreciable H<sub>2</sub> (Table 2, Fig. 4e). Some Subgroup 2a inclusions in Sample 16 show slight enrichment in higher hydrocarbons, which is evident from Raman analyses of individual inclusions and bulk gas analyses (Table 3). A vapour bubble develops on cooling, and disappears on heating, at a temperature of  $-87 \pm 5$  °C (Table 2). The homogenisation temperatures are relatively constant within different FIAs (see APPENDIX A), except for four CH<sub>4</sub>-aqueous inclusions for which the temperature range is significant, i.e., from 70 to 95 °C. A histogram showing the distribution of the homogenisation temperatures of individual inclusions (CH<sub>4</sub>-rich gas inclusions homogenising to liquid) reveals a sharp peak at ~ -87 °C (Fig. 5a); there were insufficient data to illustrate this for FIAs.

The aqueous inclusions in this group (Type IV) are smaller (5-30 µm in diameter) than the Type II inclusions, display negative crystal shapes and have a liquid/vapour ratio of ~ 90/10; about 5-10 % of the inclusions do not have a bubble at room temperature but nucleate one upon cooling (Fig. 4a and b). These inclusions freeze at a temperature of ~ -60 °C (becoming brown in colour) and upon heating undergo large-scale melting at -22.7 to -21.6 °C, which is just below the

eutectic temperature in the system NaCl-H<sub>2</sub>O (-21.1). Commonly, the ice melts completely at this temperature, leaving behind hydrohalite, which decomposes at temperatures between -22 and 0 °C. In some cases, however, the hydrohalite decomposes at the eutectic temperature, and the remaining ice melts at temperatures in the range -22 to -12 °C. The corresponding mean salinity of the aqueous FIAs varies between 19 and 29 wt.% NaCl eq. (Fig. 3, APPENDIX A) and their overall mean salinity is 23 wt.% NaCl eq. (Table 2).

The mean homogenisation temperature of the aqueous FIAs ranged between 106 and 121 °C (APPENDIX A) and the overall mean homogenisation temperature was 114 °C (Table 2); about 20% of the aqueous inclusions failed to homogenise and decrepitated when heated above 140-150 °C.

In some cases, Group 2a inclusions (aqueous, carbonic, and aqueous-carbonic) are surrounded by numerous tiny inclusions (< 1-2 µm in diameter), which we interpret to represent the product of re-equilibration or more specifically ‘implosion haloes’ (Fig. 4b). This phenomenon is discussed further in a later section of the paper.

Aqueous-carbonic (Type V) inclusions in Subgroup 2a are characterised by variable aqueous/carbonic ratios. Typically, however, the carbonic phase is dominant. The aqueous phase exhibits the same behaviour as the liquid in aqueous inclusions (Type IV); the ice melts mainly at the eutectic temperature. The behaviour of the carbonic phase is difficult to observe because of the crystallisation of ice and hydrohalite, which imparts a dark brown colour to the inclusions. However, in the four inclusions for which homogenisation of the carbonic phases could be

observed, this occurred at  $\sim -84.4$  °C, confirming that they consist dominantly of CH<sub>4</sub> (APPENDIX A).

#### **Subgroup 2b**

Inclusions belonging to Subgroup 2b are found in quartz from the cores of partially altered pegmatites (Sample 13) and also in early fluorite within hypersolvus granite (Sample 204794). The carbonic (Type II) inclusions are similar in size and shape to carbonic inclusions of Subgroup 2a, i.e., they are dark, mainly spherical and are large (15-40 µm). Like those of Subgroup 2a, the Type II inclusions in Subgroup 2b are composed mainly of CH<sub>4</sub>. However, unlike Type II inclusions in Subgroup 2a, they do not contain H<sub>2</sub> but have significant proportions of higher hydrocarbons (Fig. 4e). As is evident from Figure 5a, the individual Type II inclusions (there were insufficient inclusions to illustrate these data in terms of FIAs) homogenised over a broad range of temperature with a maximum at  $\sim -75$  °C. Based on data for FIAs (APPENDIX A), the range of homogenisation temperatures is from -80.4 to -72.2 °C for inclusions that homogenise to liquid, from -71.9 to -70.5 °C for inclusions showing critical homogenisation and from -61 to -24 °C for inclusions that homogenise to gas (APPENDIX A). With the exception of late inclusions that homogenise to vapour, the variations in the homogenisation temperature within different FIAs are not significant (APPENDIX A). However, the modes of the homogenisation temperatures differ significantly for different FIAs. In all cases, the homogenisation temperature was higher than the critical temperature for pure methane (-82.6 °C). This is interpreted to reflect the presence of higher hydrocarbons (critical temperatures for ethane and propane are 32.2 and 96.7 °C, respectively) and is consistent with the results of Raman analyses, which yielded spectra with peaks for ethane and propane (Fig. 4e). Primary



Type II and V inclusions (Fig. 4c) tend to homogenise to liquid, whereas later secondary inclusions (Fig. 4d) tend to homogenise to gas and at higher temperature; Raman analyses revealed higher contents of higher hydrocarbons in the latter inclusions.

Aqueous inclusions (Type IV) in Subgroup 2b, like their counterparts in Subgroup 2a, freeze at ~ -60 °C and are brown when frozen, but have distinctly lower salinity. The mean salinity of Type IV FIAs ranges from 10.4 to 18.4 wt.% NaCl eq. (Fig. 3, APPENDIX A) and the median salinity for the FIAs is 13.2 wt.% NaCl eq. in Sample 13, and 16.1 wt.% NaCl eq. in Sample 204794 (Table 2). Salinity variations within a single FIA are not significant (APPENDIX A). The liquid/vapour ratio is typically 70/30 compared to 90/10 in Type IV inclusions in Subgroup 2a, although inclusions with a ratio of 90/10 are also observed. Inclusions with the higher liquid/vapour ratio generally homogenised at temperatures between 85 to 128 °C and, if not, decrepitated when heated above 150 °C. Mean homogenisation temperatures within different FIAs are appreciable, i.e., they vary by 2 to 43 °C (APPENDIX A). Inclusions with the lower liquid/vapour ratio homogenised at higher temperature, i.e., 200 to 221 °C (APPENDIX A) and showed less tendency to decrepitate.

Aqueous-carbonic (Type V) inclusions in Subgroup 2b have variable aqueous/carbonic ratios, although the carbonic phase is generally dominant (Fig. 4c). The high gas/liquid ratio precluded precise estimation of the salinity of the aqueous phase in Type V inclusions. In many of the inclusions, the gas was of low density, precluding observation of their homogenisation. However, the gas was shown from Raman analyses to be composed mainly of CH<sub>4</sub>.

### ***Group 3***

Group 3 comprises a population of spatially associated Type III, IV, V, VI-1 and VI-2 inclusions (Table 2 and Fig. 6). These inclusions are found in quartz of the cores of altered pegmatites (Samples 11, SL-11-43 and SL-11-45) and vein quartz (Sample 2, see Table 1). They exhibit a random 3D distribution (Fig. 6a) and are interpreted to be primary. Inclusions located in close proximity to one another were assumed to constitute a single FIA, i.e., inclusions trapped at the same time. In some cases, the inclusions occur along sets of curved surfaces roughly parallel to grain boundaries. These surfaces are interpreted to represent growth zones and the inclusions in them to be primary; they are readily distinguished from the randomly oriented healed fractures that host secondary inclusions. The earlier curved surfaces (which have a smaller radius of curvature) are dominated by Type VI-2 inclusions and the later surfaces (with a larger radius of curvature) by Type V inclusions (Fig. 7).

Although Group 3 does not contain the carbonic Type II inclusions observed in Group 2, the Type III inclusions (dark, 25-50  $\mu\text{m}$  in diameter, Fig. 6a) that are present are very similar in appearance to Type II inclusions. However, they are generally empty (no peaks were observed during Raman analyses) and only in a few cases were traces of  $\text{CO}_2$  and  $\text{CH}_4$  identified (Fig. 8a). Moreover, their appearance is unchanged, even when cooled to  $-180^\circ\text{C}$ . Many of these inclusions display evidence of natural decrepitation in the form of numerous radiating fractures.

The Type IV (aqueous) inclusions are typically smaller (10-25  $\mu\text{m}$ ) than the Type III inclusions (Fig. 6a) and in most cases have a liquid/vapour ratio of  $\sim 90/10$ , although inclusions with smaller ratios were also observed. Some of the aqueous inclusions in this group contain only

liquid at room temperature but a vapour bubble appears on cooling. The salinity of the Type IV inclusions is lower than in both Groups 1 and 2, and varies considerably among different FIAs, although within a single FIA it is relatively constant. The mean salinity of Type IV inclusions in FIAs ranges from 5.1 to 21.5 wt.% NaCl eq. (Fig. 3, APPENDIX A) and the overall median salinity is 10, 9 and 11 wt.% NaCl eq. in Samples 11, SL-11-43 and SL-11-45, respectively (Table 2). These inclusions tend to decrepitate at relatively low temperature prior to homogenisation (150 °C or lower). Moreover, some of them decrepitate during freezing (compare Fig. 6b and c). Homogenisation temperatures were obtained for only six inclusions from a population of 67 Type IV inclusions. These inclusions homogenised at a temperature of ~78 °C (APPENDIX A). The remaining inclusions either decrepitated or the heating experiment was terminated to avoid mass decrepitation.

Type V inclusions in Group 3 commonly have “implosion haloes”. As is the case for Type V inclusions in Group 2, they have variable aqueous/carbonic ratios, but unlike the Group 2 inclusions, the carbonic phase is subordinate to the aqueous phase (especially in inclusions with ‘implosion’ haloes). Compositionally, the carbonic phase varies from a mixture of CO<sub>2</sub> and CH<sub>4</sub> (± H<sub>2</sub>, ± higher hydrocarbons) in Sample 11 to pure CO<sub>2</sub> in samples SL-11-43, SL-11-45 and 2 (Fig. 8b). Attempts to determine the composition of inclusions forming the ‘implosion’ haloes by Raman spectroscopy failed, i.e., neither H<sub>2</sub>O or carbonic species were detected.

Average temperatures (for FIAs) of homogenisation of the carbonic phase (to liquid) vary from -5.8 °C (median) for Sample 11 to 13.3 °C for Sample 2 and between 23.9 and 28.0 °C for Samples SL-11-43 and SL-11-45 (APPENDIX A). Figure 5b shows the distribution of homogenisation temperatures for individual inclusions. The carbonic phases of some inclusions

in Sample 2 also homogenise critically at 30.7 °C and to vapour at 28 °C (APPENDIX A). None of the Type V inclusions homogenised completely prior to decrepitating at a temperature of ~140°C. Type V inclusions freeze to ice (colourless) and clathrate at ~ -35 °C. The ice melts at temperatures between -7.1 and -3.6 °C (APPENDIX A) and the clathrate between 6.5 and 10.0 °C (APPENDIX A). The salinity, based on the temperature of clathrate melting, ranges from 4.2 to 4.7 wt.% NaCl eq. (Fig. 3, Table 2).

Type VI-1 inclusions are aqueous-carbonic and contain a crystal before being heated (in rare cases, two crystals were observed). In ~ 95 % of cases, the crystal is nahcolite (inset in Fig. 6h). This was confirmed through Raman analysis (Fig. 8c). Calcite and fluorite were detected in a very small number of opened inclusions using SEM-EDS analyses. The size of the nahcolite crystal varies among inclusions but typically occupies from a quarter to half of the inclusion volume. This variation in size suggests that it is a trapped solid. After repeated cooling and heating of the inclusions, the volume of nahcolite increases (compare Fig. 6h and i). The composition of the gas (Fig. 8c) varies from  $\text{CH}_4 \pm \text{H}_2$  to  $\text{CH}_4 \pm$  higher hydrocarbons.

Type VI-2 inclusions are also aqueous-carbonic but only develop a solid after repeated cooling-heating cycles. The solid comprises fine-grained aggregates of nahcolite (identified using Raman spectroscopy, Fig. 8d). Examples of these inclusions are illustrated in Figure 6 before (Fig. 6d) and after (Fig. 6e) a cooling-heating cycle. Nucleation of nahcolite is typically sluggish so that the amount of the crystallised phase in a sample gradually increases with each cooling-heating cycle. As a result, the apparent salinity decreases with each cycle due to the increase in the amount of nahcolite. For example, in one of the inclusions in Sample 11, the temperature of final ice melting was initially -9.7 °C and increased after each freezing cycle until it reached -2.5 °C,

after which further cooling did not cause any further change in this temperature. The corresponding salinity decreased from 13.6 to 4.2 wt.% NaCl eq. During heating, the newly formed nahcolite decomposed at a temperature between 70 and 95 °C, which corresponds to 14-17 wt.% of the nahcolite component in the fluid (Braitsch, 1964). The composition of the gas in the inclusions, as is the case for Type VI-1 inclusions, varies from  $\text{CH}_4 \pm \text{H}_2$  to  $\text{CH}_4 \pm$  higher hydrocarbons (Fig. 8d, Table 2) after freezing cycles and crystallisation of nahcolite.

#### ***Group 4***

Group 4 comprises only Type IV (aqueous) inclusions (Table 2). These inclusions are distributed in 3D groups and are interpreted to be primary. In one sample, SL-11-45, they were found along healed fractures crosscutting growth zones containing Group 3 inclusions (Fig. 7b). Locally the Group 4 inclusions contain a single phase at room temperature but nucleate a bubble upon cooling. They freeze at  $\sim -35$  °C and are colourless when frozen. The salinity of the inclusions (the two-phase inclusions and those nucleating a vapour bubble on cooling) varies greatly among different FIAs, i.e., from 0.8 to 16.1 wt.% NaCl eq. (APPENDIX A). Variations in salinity within a single FIA are not significant (APPENDIX A). The overall median FIA salinity for Samples 7, SL-11-14, SL-11-22 and SL-11-45 is 13, 4, 4 and 9 wt.% NaCl eq. (Table 2).

About 90 % of Group 4 inclusions decrepitated prior to homogenisation at a temperature between  $\sim 150$  and 200 °C. Inclusions that did not decrepitate homogenised at  $146 \pm 30$  °C (Table 2). ‘Implosion haloes’ are less common for Group 4 aqueous inclusions than for Group 3 inclusions.

## 436 **Group 5**

437 Group 5 comprises Type IV and VI-3 (aqueous) inclusions (Table 2), and is common in the  
438 quartz of altered subsolvus granite (Samples 204739 and 204741) and pegmatite (Samples SL-  
439 11-14, SL-11-22 and SL-11-45). These inclusions help define the margins of pseudomorphs but  
440 also occur within the pseudomorphs (Group 5a, Fig. 9a and b). As well, they are distributed in  
441 3D groups within the latest generation of quartz (filling miarolitic cavities, Group 5b, Fig. 9c),  
442 and in some cases occur along healed fractures (Group 5c, Fig. 9d) that crosscut primary Group 4  
443 inclusions. Some of the inclusions (Group 5c) were trapped in narrow tubes, which crosscut  
444 growth zones (Fig. 7d). These tubes likely originated from line defects, i.e., dislocations, which  
445 were enlarged (dissolved) by hydrothermal fluid (possibly rich in NaOH). Formation of  
446 dislocations in quartz is a well-known phenomenon (Götze, 2009), and cavities produced by  
447 hydrothermal etching of these dislocations have been used for the synthesis of fluid inclusions  
448 (Balitsky et al., 2007; Balitskaya and Balitsky, 2010).

449 Type IV and VI-3 inclusions in Group 5 are small (5-10  $\mu\text{m}$  in diameter), have irregular shapes  
450 (Fig. 9) and constant liquid/vapour ratios ( $\sim 95/5$ ). The Type VI-3 inclusions in Group 5a contain  
451 minerals typical of the pseudomorphs, i.e., in gittinsite-quartz-zircon pseudomorphs, the solid in  
452 the inclusions is zircon and in rare cases pyrochlore, whereas in titanite-quartz $\pm$ fluorite  
453 pseudomorphs they are titanite and fluorite (Table 2, Sample 204741). Group 5b inclusions  
454 commonly contain microcline or albite (Table 2, Sample 204739). In both Group 5a and 5b, the  
455 solids occupy from 10 to 90 % of the inclusion volume. The vapour bubble is composed of  $\text{H}_2\text{O}$ ;  
456 in a few Group 5b inclusions, traces of  $\text{H}_2$  were detected. The inclusions freeze at  $\sim -60^\circ\text{C}$  to a  
457 dark brown phase(s). The two types of inclusions (Type IV and VI-3) have similar salinity, of 17

to 27 wt.% NaCl eq. (Fig. 3, Table 2). In two inclusions, very low initial ice-melting temperatures (~-50 °C) indicated the presence of divalent cations, most likely Ca. These inclusions had the highest salinity of any of the inclusions that were analysed microthermometrically. The homogenisation temperature of the Type IV and Type VI-3 inclusions (FIA data) is in the range 71-125 °C (APPENDIX A).

### ***Bulk gas analyses***

Quartz from ten samples was analysed for its bulk gas composition (Table 1). These samples were chosen using the criterion that a single inclusion group should be dominant. The exception is Sample 7, which contains two inclusion populations, Groups 4 and 5, and was selected because none of the many samples examined contained Group 4 inclusions, without a large proportion of inclusions of another group. It thus needs to be emphasised that the data for Group 4 inclusions are actually a composite of data for Group 4 and 5 inclusions.

Three groups of samples were distinguished (Table 3), namely samples rich in CO<sub>2</sub> (2 and 11), CH<sub>4</sub>-rich samples (4, 13, 16 and 204722) and samples enriched mainly in the aqueous component (7 and 204739). The results are consistent with our microthermometric and laser-Raman observations, i.e., samples dominated by Group 3 inclusions are CO<sub>2</sub>-rich, samples dominated by Group 1 and 2 inclusions are CH<sub>4</sub>-rich, and samples mainly containing Group 4 and 5 inclusions are H<sub>2</sub>O-rich (Table 3). Sample 13 is extremely rich in higher hydrocarbons (C<sub>2</sub> to C<sub>6</sub>), with these species making up 5.3 mol.% of the incondensable gas fraction compared to between 0.007 and 1.2 mol.% in the other samples (Table 3). This result is consistent with the results of Raman analyses presented earlier showing that Type II inclusions in Sample 13 have

appreciable proportions of higher hydrocarbons (Fig. 4e). In addition to the carbonic species, the bulk gas analyses also detected appreciable N<sub>2</sub>, up to 2.4 mol.% in CH<sub>4</sub>-rich samples and 1.6 mol.% in H<sub>2</sub>O-rich samples (Table 3). Finally, we note that Sample 204722 has an extremely high hydrogen content and that the H<sub>2</sub> proportion is also high in three of the four CH<sub>4</sub>-rich samples, and in one of the H<sub>2</sub>O-rich samples (204739) (Table 3).

## Discussion

### *Re-equilibration and decrepitation*

One of the most striking features of the inclusions investigated in this study is the presence of tiny satellite inclusions, so-called ‘implosion’ haloes, around many of them, i.e., around Type IV inclusions in Groups 1, 2 and 3, and Type V and VI inclusions in Group 3 (Fig. 6). Based on observations from natural settings (Vityk et al., 1995) and laboratory experiments (Sterner and Bodnar, 1989; Bakker and Jansen, 1994; Vityk and Bodnar, 1995; Vityk et al., 2000; Vasyukova and Fonarev, 2006), these textures are interpreted to be a product of the response of the host mineral to isobaric cooling. They develop as a result of re-crystallisation of the quartz around the inclusion due to the strain caused by the pressure difference between the inclusion and the host crystal, the so-called effective pressure (Bakker and Jansen, 1994). The effective pressure is the driving force for the dissolution-precipitation mechanism, which dissolves silica around the inclusion and re-precipitates it within the inclusion (Bakker and Jansen, 1994). The extent of re-crystallisation depends on the pressure gradient and the solubility of quartz in the trapped fluid. For example, aqueous inclusions are expected to be more strongly affected by isobaric cooling because they undergo more abrupt pressure decrease (their isochores are steeper) and the



solubility of quartz in the aqueous fluid is high. The pressure gradient for CO<sub>2</sub>-inclusions is higher than for CH<sub>4</sub>-inclusions, but due to the extremely low solubility of quartz in both of these fluids, dissolution and precipitation of this phase are negligible. Therefore, pure CO<sub>2</sub> and CH<sub>4</sub> inclusions cannot re-equilibrate and will decrepitate when the strain produced by the effective pressure is too high. However, aqueous-carbonic inclusions are able to re-equilibrate and aqueous-CO<sub>2</sub> inclusions will be affected more strongly than aqueous-CH<sub>4</sub> inclusions. This is exactly what was observed in this study, i.e., whereas most aqueous and CO<sub>2</sub>-aqueous inclusions are surrounded by large ‘implosion’ haloes (Fig. 6), there is much less evidence for such re-equilibration around CH<sub>4</sub>-aqueous inclusions (Fig. 4).

Re-equilibration led to a decrease in the temperature of homogenisation, which explains the very low homogenisation temperature of most Group 1, 2 and 3 aqueous inclusions. The tendency of the inclusions (even those without detectable incondensable gases like CO<sub>2</sub> and CH<sub>4</sub>) to decrepitate easily is also consistent with their re-equilibration. This is because the development of numerous tiny voids around the inclusions weakens the host quartz and sharply reduces its capacity to withstand the pressure increases that accompany heating of the inclusions.

### ***Fluid evolution***

The earliest fluid preserved in the rocks at Strange Lake is represented by Group 1 inclusions, i.e., fluid inclusions that are spatially associated with melt inclusions. These inclusions were observed in Samples 204722, 16 and 4, which are from the outer parts of unaltered pegmatites containing a coarse-grained intergrowth of quartz, K-feldspar and arfvedsonite. From the spatial distribution of the fluid and melt inclusions (they occur in the same growth zones in quartz, see

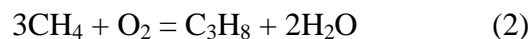
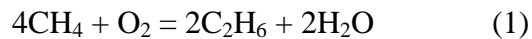
Fig. 2b), we conclude that the fluid coexisted with the pegmatite melt at the time of its entrapment and that it therefore exsolved from this melt. The nature and microthermometric behaviour of the Group 1 inclusions indicates that the fluid contained aqueous and carbonic components and after phase separation the aqueous phase had a salinity of ~25 wt.% NaCl eq. (Table 2).

The presence of Group 1 CH<sub>4</sub>-rich inclusions devoid of CO<sub>2</sub> (Table 2, Fig. 2b) and the bulk gas composition of Sample 204722 (Table 3) indicate that the carbonic component probably was dominated by CH<sub>4</sub> and H<sub>2</sub>. Growth zones containing Group 1 inclusions are cut by healed fractures containing Group 2a inclusions (Fig. 2d), which indicates their later origin. The latter inclusions are common in Sample 204722, where they are secondary (Fig. 2d), and in Sample 16, where they are mostly primary. Both samples are unaltered and were taken from the border zones of pegmatites (Table 1). The salinity of aqueous Group 2a inclusions is ~ 23 wt.% NaCl eq. (Table 2), which is very similar to that of the aqueous phase of Group 1 inclusions.

The composition of the carbonic component of Group 2a inclusions is similar to that of the carbonic component of Group 1 inclusions (CH<sub>4</sub>-dominant, Table 2). However, the proportion of H<sub>2</sub> in the bulk gas of Sample 204722, in which Group 1 inclusions predominate, is much higher than in Sample 16, which mainly contains Group 2a inclusions (Table 3). We therefore conclude that the Group 2a fluid evolved from the exsolved magmatic fluid (Group 1), and that it did so by becoming slightly more oxidised than the original fluid (lower H<sub>2</sub> content).

A further stage in the evolution of the fluid is recorded by Group 2b inclusions, trapped in Sample 13, which was taken from a partially altered pegmatite (arfvedsonite is weakly altered to

aegirine along its rims). These inclusions are similar in appearance and distribution, as well as in composition, to Group 2a inclusions (CH<sub>4</sub>-dominated carbonic inclusions and NaCl-rich aqueous inclusions), except that the carbonic inclusions contain significant proportions of higher hydrocarbons (C<sub>2</sub> to C<sub>6</sub>) and the aqueous inclusions have lower salinity (13 wt.% NaCl eq. versus 23 wt.% NaCl eq. in Group 2a inclusions, Table 2). A high content of higher hydrocarbons in similar inclusions was also reported by Salvi and Williams-Jones (1997), who proposed that magnetite-catalysed Fischer-Tropsch synthesis, which transforms CO and CO<sub>2</sub> into CH<sub>4</sub> and higher hydrocarbons, was responsible for the formation of the hydrocarbons. Our fluid inclusion data, however, indicate that the higher hydrocarbon species are associated with a CH<sub>4</sub>-dominated fluid free of CO<sub>2</sub> or CO, and that the earlier Groups 1 and 2a inclusions are also CO<sub>2</sub>-(CO)-free. We conclude, therefore, that Fischer-Tropsch synthesis was probably not responsible for the formation of the higher hydrocarbon species in Group 2b inclusions. Instead, we propose that these hydrocarbons formed due to cooling-induced oxidation, and that oxidative coupling of methane was responsible for the conversion of CH<sub>4</sub> into C<sub>2</sub> to C<sub>6</sub> hydrocarbons via the reactions:



In general, oxidation of CH<sub>4</sub> leads directly to the formation of CO<sub>2</sub> via the reaction, CH<sub>4</sub> + 2O<sub>2</sub> = CO<sub>2</sub> + 2H<sub>2</sub>O. However, if oxidation is inhibited, for example, through the consumption of oxygen in another reaction, formation of CO<sub>2</sub> will be replaced by that of C<sub>2</sub>H<sub>6</sub> and C<sub>3</sub>H<sub>8</sub> (Reactions 1 and 2). We propose that oxidation was inhibited due to the replacement of

arfvedsonite by aegirine (a relatively early hydrothermal mineral), which consumed oxygen according to the reaction:



Owing to this alteration, the  $f\text{O}_2$  was too low to produce  $\text{CO}_2$  from  $\text{CH}_4$ , but high enough to trigger oxidative coupling of methane (Reactions 1 and 2) and therefore, facilitate formation of higher hydrocarbons.

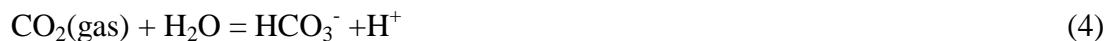
As mentioned above, evolution from the Group 2a fluid to the Group 2b fluid was accompanied by a decrease in salinity (from 23 to 13 wt.% NaCl equivalent). Inasmuch as arfvedsonite is a major igneous phase and was altered extensively to aegirine, we propose that the decrease in salinity was due dilution of the fluid by the large amount of  $\text{H}_2\text{O}$  produced during this alteration (Reaction 3).

Although we did not observe textural relationships that might indicate the relative timing of entrapment of Group 2b and 3 inclusions, it seems likely that Group 3 inclusions were trapped later because they occur in more altered samples (Samples 11, SL-11-43, SL-11-45 and 2, Tables 1 and 2). If this were the case, it would indicate a progressive relative increase of  $f\text{O}_2$  from Group 2b, because in Group 3 inclusions the gas is composed mainly of  $\text{CO}_2$ . It would also indicate that  $f\text{O}_2$  was no longer buffered by Reaction 3 and that alteration of arfvedsonite to aegirine had ceased before entrapment of Group 3 inclusions. Gysi et al (2016) showed that arfvedsonite in the Strange Lake granites and pegmatites underwent three types of alteration, namely pervasive replacement by aegirine, core-replacement by hematite and rim replacement by aegirine  $\pm$  hematite. We propose that these different types of alteration reflect different physico-

chemical conditions, and that at relatively high temperature arfvedsonite was replaced by aegirine, whereas at lower temperature it was replaced by aegirine and/or hematite.

To summarise, we propose that the Group 3 fluid evolved from the Group 2b fluid by cooling-induced oxidation due to the cessation of alteration of arfvedsonite by aegirine. In view of this conclusion, we interpret the presence of significant CH<sub>4</sub> in the CO<sub>2</sub>-rich gas of Sample 11 to indicate that the Group 3 fluid in this sample was trapped earlier than in the other samples.

In addition to containing appreciable CH<sub>4</sub>, Group 3 inclusions in Sample 11 also commonly contain accidentally trapped nahcolite crystals (Type VI-1 inclusions), indicating that nahcolite saturated in the fluid prior to or during transformation of the Group 2b fluid to the Group 3 fluid. Significantly, nahcolite is not present in the other samples containing Group 3 fluid inclusions but crystallised during freezing (Type VI-2 inclusions). In the case of Sample SL-11-45, it precipitated in inclusions trapped along early growth zones (Type VI-2 inclusions), whereas late growth zones in this sample are dominated by CH<sub>4</sub>-free aqueous-CO<sub>2</sub> inclusions (Type V), in which nahcolite did not form on freezing. These observations indicate that the Group 2b fluid evolved by: 1) oxidising CH<sub>4</sub> (and higher hydrocarbons) to CO<sub>2</sub> and saturating the fluid with nahcolite (Type VI-1 inclusions); 2) further oxidising CH<sub>4</sub> and saturating the fluid with nahcolite but only after entrapment and freezing (Type VI-2 inclusions); and 3) finally forming a CH<sub>4</sub>-free aqueous-CO<sub>2</sub> fluid that even after entrapment and freezing did not crystallise nahcolite (Type V inclusions). We propose that nahcolite precipitated as a result of the reactions:



which decreased pH, eventually causing the fluid to evolve from the predominance field of  $\text{HCO}_3^-$  to that of  $\text{H}_2\text{CO}_3$  (point B Fig. 10), and cease precipitation of nahcolite, except after entrapment and freezing (Type VI-2 inclusions) (red arrow, Fig. 10). The pH continued to decrease after precipitation of nahcolite terminated because of the production of additional  $\text{CO}_2$  (through oxidation of  $\text{CH}_4$ ), which pushed the fluid even further into the predominance field of  $\text{H}_2\text{CO}_3$  (line C-D, Fig. 10), thereby preventing precipitation of nahcolite even after freezing (Type V inclusions).

An observation of some interest is that the temperature of dissolution of nahcolite aggregates in Type VI-2 inclusions (75-90 °C) is indicative of a fluid containing 14-17 wt.% dissolved  $\text{NaHCO}_3$ , which is significantly more than is needed for nahcolite saturation (6.27 wt.% in a NaCl-free fluid and 1.06 in a NaCl-saturated fluid; (Marion, 2001). We speculate that such oversaturation of the fluid with respect to nahcolite was governed by higher concentrations of  $\text{CO}_2$  in the fluid before freezing, which could have been caused by the presence of a  $\text{CO}_2$  gas phase in the inclusions.

The evolution of the carbonic component of the fluid from Group 2b to Group 3 (2b→VI-1→VI-2→V) was accompanied by a progressive decrease in the salinity from ~13 to ~4 wt.% NaCl eq. (compare salinity of the fluid 2b and 3). We propose, as we did to explain the decrease in salinity from the Group 2a fluid to the Group 2b fluid, that this was due to dilution caused by the  $\text{H}_2\text{O}$  produced during the alteration of arfvedsonite, but in this case to aegirine and hematite or hematite alone.

Group 4 inclusions post-dated Group 3 inclusions, as shown by their crosscutting relationships in Sample SL-11-45 (see Fig. 7). Unlike Group 3 inclusions, which contain a gas dominated by CO<sub>2</sub>, Group 4 inclusions do not contain incondensable gases. However, the salinity of the Group 4 fluid is very similar to that of the Group 3 fluid (Table 2), which suggests that the Group 4 inclusions represent the aqueous part of the immiscible CO<sub>2</sub>-H<sub>2</sub>O pair. Alternatively, Group 4 inclusions might represent a fluid that evolved from the Group 3 fluid, and lost CO<sub>2</sub> by fluid-rock interaction. Some CO<sub>2</sub> may have been consumed to form secondary bastnäsite-(Ce) from primary REE-silicates as described in Vasyukova and Williams-Jones (2016) and also in precipitating minor interstitial calcite.

The Group 5 fluid is represented by secondary inclusions trapped along healed fractures crosscutting Group 4 inclusions (sample SL-11-14, Fig. 9d), inclusions defining the boundaries of pseudomorphs after primary titanosilicate and zirconsilicate minerals (Fig. 9a) and primary inclusions in secondary minerals (Fig. 9c). Group 5 inclusions are aqueous without a detectable carbonic gas component and have significantly higher salinity than Group 4 fluid inclusions, i.e., 18.4-27 wt.% NaCl eq. (Table 2), which is very close to the salinity of the Group 1 and 2a fluids. We propose that the Group 5 fluid evolved from the Group 4 fluid by additional fluid-rock interaction, notably the formation of the Al-, K- and Fe-phyllsilicates described in Gysi and Williams-Jones (2013), which involved the consumption of H<sub>2</sub>O and would have resulted in a matching increase in the salinity of the fluid.

### *Pressure-temperature conditions*

The textural evidence presented earlier indicates a prolonged period of isobaric cooling. During this period, the composition of the gas changed from CH<sub>4</sub>-rich (and CO<sub>2</sub>-free) to CO<sub>2</sub>-dominated, which indicates a corresponding increase in the oxidation state. This does not mean, however, that oxygen fugacity increased, because at constant oxygen fugacity a decrease in temperature will favour the formation of oxidised species. We propose that isobaric cooling and resultant oxidation and fluid-rock interaction controlled fluid evolution in the Strange Lake pluton. Here, we estimate the evolving pressure-temperature conditions during which the different fluid groups described earlier were trapped.

As has been mentioned, the hydrothermal history of the Strange Lake pluton began with the exsolution of a NaCl-rich brine from the magma. Direct evidence of this separation is provided by the coexistence of saline Na-rich fluid inclusions and melt inclusions in the same growth zones of pegmatite-hosted quartz (Group 1). Unfortunately, the Type 1a inclusions re-equilibrated during isobaric cooling and therefore cannot be used to determine the P-T conditions of this phase separation.

Pressure-temperature conditions during the entrapment of Group 2 inclusions were calculated using the intersection of the isochores of the immiscible CH<sub>4</sub> (Type II) and aqueous fluid (Type IV) endmembers. The CH<sub>4</sub>-rich inclusions contain 97 mol.% CH<sub>4</sub> and 3 mol.% H<sub>2</sub> (estimates based on bulk gas analyses) and homogenise at a temperature of ~ -85 °C (Table 4). Unfortunately, most of our Group 2 inclusions re-equilibrated and were surrounded by implosion haloes (tiny voids), which weakened the surrounding quartz, causing the inclusions to decrepitate



prior to homogenisation. However, the Group 2 inclusions are remarkably similar to inclusions studied by Salvi and Williams-Jones (1992) and have the same salinity of ~23 wt.% NaCl eq. As a statistically meaningful proportion of their inclusions homogenised, we assumed that the homogenisation temperature mode reported by them for their analogous aqueous inclusions (340 °C) would have been the same for our Group 2 aqueous inclusions had they not decrepitated. The corresponding isochore for these inclusions crosses the isochore for the Type 2a CH<sub>4</sub>-rich inclusions at 425 °C and 1100 bar (Fig. 11, event '2', isochores a and b).

Pressure-temperature conditions of entrapment for Group 2b inclusions were also determined by calculating the intersection between the isochores of endmembers of the immiscible fluid, i.e., aqueous inclusions and CH<sub>4</sub>-rich inclusions. Although homogenisation of these inclusions occurred over a wide temperature interval, i.e., from 50 to 284 °C (based on data for individual inclusions), for the purpose of our calculations, we chose the highest temperature and considered that inclusions, which homogenised at lower temperature, had re-equilibrated during isobaric cooling. The salinity of these inclusions is 14 wt.% NaCl eq. (Table 4). It was also necessary to simplify the gas composition, as there are no PVT data for fluids containing hydrocarbons with more than two carbon atoms. We therefore assumed that the gas was composed of CH<sub>4</sub> and C<sub>2</sub>H<sub>6</sub>, and, based on the bulk gas analyses, that they were present in the ratio 0.77/0.23 (Table 3). The isochores for the aqueous and gas-rich inclusions intersect at approximately 360 °C and 1100 bar (Fig. 11, event '3', isochores c and d) consistent with our proposal that the cooling was isobaric.

Unfortunately, it was not possible to use the above method for the Group 3 inclusions, as pure CO<sub>2</sub> inclusions were not observed. However, a rough estimate was made by assuming that the

density of the CO<sub>2</sub> at the time of entrapment was close to that of CO<sub>2</sub> in Type V inclusions from SL-11-45 (the CO<sub>2</sub> phases in these inclusions homogenised at ~25 °C, Table 4). The corresponding isochore crosses the isobaric cooling path at ~ 310 °C (point '6' in Figure 11), suggesting that oxidation of CH<sub>4</sub> to CO<sub>2</sub> was complete by the time that this temperature was reached. It is important, nevertheless, to note that the above assumption likely resulted in an overestimation of the temperature of entrapment and thus the temperature of 310 °C represents a maximum for the complete conversion of CH<sub>4</sub> to CO<sub>2</sub>.

The density and an isochore for Group 4 inclusions were determined assuming a salinity of 4 wt.% NaCl eq. and a homogenisation temperature of 160 °C (based on individual inclusion analyses, Table 4). Assuming that the cooling remained isobaric, the Group 4 inclusions were trapped at ~ 225 °C and 1100 bar (isochore 'e' and point '4' in Figure 11).

An isochore for the Group 5 inclusions was calculated from the mean homogenisation temperature of 110 °C and a salinity of 19 wt.% NaCl eq. (Table 4). This isochore intersects the isobaric cooling path at 160 °C (isochore 'f' and point '5' in Figure 11).

### ***Oxygen fugacity***

According to estimates made by (Salvi and Williams-Jones, 1992, 1997; Gysi and Williams-Jones, 2013), the oxygen fugacity of the system was between 2 and 5 log units below the QFM buffer at the onset of fluid exsolution and the cessation of arfvedsonite crystallisation. The subsequent path taken by oxygen fugacity is less clear. It is attractive to argue that the widespread evidence for the replacement of arfvedsonite by aegirine indicates a relative increase in oxygen fugacity and its buffering by this assemblage. However, as was shown by Evans

(2007) and pointed out by Gysi and Williams-Jones (2013), arfvedsonite cannot transform directly to aegirine (in a closed system) at subsolidus conditions (i.e., below 600 °C), without first forming riebeckite, for which there is no evidence. Gysi and Williams-Jones (2013) therefore proposed two explanations for the observed alteration of arfvedsonite to aegirine. The first of these was rapid undercooling to limit fluid-rock interaction and keep oxygen fugacity roughly constant, thereby allowing aegirine to become stable at a temperature of 300 to 350 °C. The second explanation envisaged rock buffering of oxygen fugacity to lower values as temperature decreased, until mixing with an external oxidising fluid abruptly raised oxygen fugacity, stabilising aegirine at the expense of arfvedsonite. This latter explanation is consistent with the interpretation of Salvi and Williams-Jones (1997) that the CO<sub>2</sub>-bearing fluid inclusions at Strange Lake resulted from oxidation of the magmatic hydrothermal fluid by a meteoric fluid. In the succeeding paragraphs, we evaluate the evolution of the oxygen fugacity of the system based on the compositional data for the different fluid groups gathered in the current study.

Thermodynamic calculations were performed for a mixture of the following gases, CH<sub>4</sub>, H<sub>2</sub>, O<sub>2</sub>, CO<sub>2</sub>, CO, H<sub>2</sub>O, C<sub>2</sub>H<sub>6</sub> and C<sub>3</sub>H<sub>8</sub>, all of which are known to occur in the fluid inclusions at Strange Lake. Nitrogen was not considered because, although it was detected in bulk gas analyses (Table 3 in our study and also in Salvi and Williams-Jones, (1992, 1997), we did not detect it in Raman analyses of individual inclusions, and therefore do not know its distribution among the different inclusion groups. Hydrocarbons with greater than three carbon atoms, likewise, were not considered, in this case, because of a lack of thermodynamic data. We assumed, as did Salvi and Williams-Jones (1997), that at  $\leq 350$  °C the mole fraction of H<sub>2</sub>O vapour in the gas phase is about ~0.01, that it increases with increasing temperature, and equals 0.2 and 0.4 at 425 and 500 °C

(Table 5). In the absence of data on the solubility of H<sub>2</sub>O-NaCl vapour in CH<sub>4</sub> gas at high temperature, we assumed that at 350 °C, the solubility of H<sub>2</sub>O in CH<sub>4</sub> gas is the same as that of CH<sub>4</sub> in the corresponding brine (Duan et al., 1992a), and that the solvus of the system CH<sub>4</sub>-H<sub>2</sub>O-NaCl is roughly parallel to, but 100 °C higher, than that of the system CO<sub>2</sub>-H<sub>2</sub>O-NaCl for the same salinity (Holloway, 1984).

Using the set of equations presented in APPENDIX B, we expressed the fugacity of each gas in terms of  $f_{O_2}$  and  $f_{H_2O}$ , then fixed the latter using the assumptions mentioned above and adjusted  $f_{O_2}$  until the fluid composition was as close as possible to that of each of the groups of fluid inclusions (Tables 3 and 5). All calculations were performed for a pressure of 1100 bars and the temperatures reported in the previous section, i.e., 500 °C for Group 1, 425 °C for Group 2a, 360 for group 2b, 300 °C for Group 3 and 225 °C for Group 4 inclusions.

Our calculations show that the  $\log f_{O_2} - T$  path followed by fluids with the compositions observed in this study began with a  $\log f_{O_2}$  value at 500 °C, which is 7.3 units below the QFM buffer (point ‘1’ in Fig. 12). At 425 and 360 °C, the  $\log f_{O_2}$  evolved to 6.2 and 2.8 units below QFM, respectively (points ‘2a’ and ‘2b’ in Fig. 12) and at ~310 °C crossed the predominance boundary of CH<sub>4</sub> and CO<sub>2</sub> (~1.7 log units below QFM) into the CO<sub>2</sub>-dominant field (Fig. 12). The values of points ‘1’ to ‘4’ are reported in Table 5 together with two additional points, interpolated for temperatures of 325 and 350 °C.

According to the calculations, the proportion of C<sub>2</sub>-C<sub>3</sub> hydrocarbons in the carbonic phase increases with cooling from 0.01 and 0.02 mol.% at 500 and 425 °C, to 2.3 and 2.7 mol.% at 360 and 350 °C, respectively, to a maximum of 5.9 mol. % at 325 °C. It then decreases precipitously

750 to 0.1 mol.% at 300 °C (Table 5). The proportion of methane reaches a maximum of 96.8 mol.%  
 751 at 425 °C and decreases with both higher and lower temperature. At 500 °C, the proportion of  
 752 CH<sub>4</sub> is 83 mol.%, whereas at 360, 350 and 325 it decreases to 95.5, 91.4 and 48 mol.%  
 753 respectively, and at 300 °C, it is only 16 mol.%; no CH<sub>4</sub> is present at temperatures lower than  
 754 275 °C. The hydrogen content is only significant at high temperature, rising from 3 mol.% at 425  
 755 °C to 16.7 mol.% at 500 °C. Carbon dioxide dominates at  $\leq 300$  °C, e.g., rising from 2.1 and 5.7  
 756 mol.% at 360 and 350 °C to 45.7, 83.4 and 99.99 at 325, 300 and 225 °C, respectively (Table 5).

757 These calculations demonstrate convincingly that gases in the proportions observed in analyses  
 758 of the bulk gas composition of the Strange Lake samples can co-exist in equilibrium. The only  
 759 exception is Sample 13, which has an extremely high content of C<sub>2</sub> to C<sub>6</sub> hydrocarbons (~27  
 760 mol.% excluding H<sub>2</sub>O). The fact that we were able to replicate the gas composition (except for  
 761 Sample 13) also serves to confirm our conclusion that oxygen fugacity decreased progressively  
 762 with temperature, requiring that it was at least partly buffered. We do not know what was  
 763 responsible for this buffering during the first part of the cooling path, but as Samples 4 and 16,  
 764 which trapped Group 1 and Group 1 and 2a inclusions, respectively, are unaltered, we speculate  
 765 that reaction of the exsolving gases with the crystallising magma may have played a role.  
 766 However, as has already been discussed, the subsequent buffering was the result of the alteration  
 767 of arfvedsonite to aegirine (Reaction 3), which commenced at ~360 °C and continued until ~325  
 768 °C. As this alteration was associated with the production of C<sub>2</sub> to C<sub>6</sub> hydrocarbons, we can  
 769 assume that during this period  $f_{O_2}$  was probably above the  $f_{C_2H_6}/f_{CH_4}$  and  $f_{C_3H_8}/f_{C_2H_6}$   
 770 predominance boundaries and just below that of  $f_{CO_2}/f_{C_3H_8}$  or  $f_{CO_2}/f_{CH_4}$  (Fig. 12). Oxygen

fugacity at temperatures below 300 °C was probably controlled by alteration of arfvedsonite to hematite and other reactions involving hematite.

As discussed earlier, because riebeckite is not observed at Strange Lake and textural relationships indicate direct transformation of arfvedsonite to aegirine, Gysi and Williams-Jones (2013) proposed two log  $f_{O_2}$  – T paths to avoid prior formation of riebeckite. The first of these is fast undercooling at  $f_{O_2}$  fixed 2-5 log units below the QFM buffer (Path 1, in Fig. 12). This path can be ruled out because it would lead to dominance of the gas phase by CO<sub>2</sub> at high temperature (> 450 °C), as well as during subsequent cooling, which clearly was not the case. The second path requires that  $f_{O_2}$  lie below but roughly parallel to the curve for the QFM buffer and then increase abruptly due to the introduction of oxidised meteoric fluid at ~250 °C, driving conditions into the stability field of aegirine (Path 2, in Fig. 12). This second path qualitatively explains the observed changes in the gas composition, including the production of higher hydrocarbons and finally CO<sub>2</sub>, albeit at lower temperature than predicted by our model calculations (Fig. 12). The essential difference between this path and the calculated path discussed above is that the latter does not require the introduction of an external fluid to explain the massive production of CO<sub>2</sub>.

An issue not addressed by the calculated path is how arfvedsonite was altered to aegirine without first forming riebeckite. A possible explanation is suggested by the observation that the stability relationships involving arfvedsonite, aegirine and riebeckite were determined for a closed system involving assemblages of four minerals at isobaric univariance (Ernst, 1962; Evans, 2007). At Strange Lake, however, hydrothermal alteration proceeded in an open system (Salvi and Williams-Jones, 1996; Gysi and Williams-Jones, 2013). In such an environment, assemblages

involving two minerals would have been the norm and stability relationships among arfvedsonite, riebeckite and aegirine would have been determined by the chemical potentials of their essential components. Given the high salinity of the fluid, Na was likely the most important of these components, Fe was much less important because of the relative immobility of  $\text{Fe}^{3+}$  and Si activity would have been buffered by quartz. We can determine the relative chemical potential of Na in the three minerals of interest from their compositions. If the mineral formulae of the three minerals are normalised to constant Si, it can be seen that the proportion of Na is lowest in riebeckite (2/8), intermediate in arfvedsonite (3/8) and highest in aegirine (4/8). It therefore follows that in the presence of a NaCl-rich fluid, as was the case at Strange Lake, arfvedsonite would have altered directly to aegirine rather than through an intermediate reaction involving riebeckite.

#### ***Higher hydrocarbons***

Until now, the occurrence of  $\text{C}_2$  to  $\text{C}_6$  hydrocarbons in fluid inclusions at Strange Lake has been attributed to a Fischer-Tropsch synthesis, i.e., formation of the hydrocarbons as a result of the reaction of  $\text{CO}_2$  (+CO) with  $\text{H}_2$  in the presence of magnetite as the catalyst (Salvi and Williams-Jones, 1997, 2006). The main reason that this process was proposed is that the authors were unable to explain the measured distribution of the higher hydrocarbons by reactions in the gas phase based on an equilibrium thermodynamic model. However, in constructing their model, Salvi and Williams-Jones (1997) assumed that oxygen fugacity was buffered by fluid-rock interaction to a set of values that varied with temperature parallel to those of the QFM buffer. All sets of values on, above and below the buffer that were considered by them failed to yield the measured gas composition. In contrast, the Fischer-Tropsch model, which involves breaking the

815 C-O bond and replacing it with a C-C or C-H bond, successfully reproduced the observed gas  
816 composition and, consistent with this model, the distribution of higher hydrocarbons obeyed the  
817 Shultz-Flory distribution rule.

818 In this study, we have returned to the equilibrium model, but instead of assuming that oxygen  
819 fugacity was buffered parallel to QFM, we adjusted  $f_{O_2}$  until the calculated gas composition  
820 matched the observed composition. The result was an oxidative coupling of methane to form the  
821 higher hydrocarbons ( $C_2$  and  $C_3$ ), which were not produced in the equilibrium model of Salvi and  
822 Williams-Jones (1997), because of the much more precipitous drop in  $f_{O_2}$  with temperature (Fig.  
823 12). This production of higher hydrocarbons was made possible by the replacement of  
824 arfvedsonite by aegirine (Reaction 3), which consumed oxygen, allowing formation of ethane  
825 and propane to proceed and avoid the direct oxidation of  $CH_4$  to  $CO_2$ . In support of our model,  
826 we note: 1) that higher hydrocarbon-bearing fluids were preceded by higher temperature  
827 methane-bearing fluids and postdated by lower temperature carbon dioxide-bearing fluids; 2)  
828 that the hydrocarbon-bearing fluids and other compositional groups of fluids define a path of  
829 continuously decreasing  $f_{O_2}$  (Fig. 12); and 3) that the highest concentrations of hydrocarbons are  
830 in fluids ( $CO_2$ -bearing) that formed closest to the  $CH_4/CO_2$  predominance boundary (325-360  
831 °C; Fig.12, Table 5). We also note that the Fischer-Tropsch model calls for an early  $CO_2/CO$   
832 bearing orthomagmatic fluid (Salvi and Williams-Jones, 1997), whereas the fluid inclusions  
833 associated with melt inclusions described in this study (Group 1 inclusions) are  $CH_4+H_2$ -rich and  
834 show no trace of  $CO_2$  or  $CO$ . Thus, although Fischer-Tropsch synthesis offered an attractive  
835 explanation for the formation of higher hydrocarbons, we now consider that these species were



836 the product of oxidative coupling of methane mediated by the alteration of arfvedsonite to  
837 aegirine.

### 838 ***HFSE mobilisation***

839 Our data on the evolution of the fluid at Strange Lake have allowed us to understand when and  
840 how the HFSE were remobilised. From our previous studies of the Strange Lake pluton, it is  
841 evident that the primary concentration of the REE was effected by an immiscible fluoride melt  
842 into which the REE partitioned preferentially (Vasyukova and Williams-Jones, 2014, 2016). This  
843 melt, which initially was dispersed as small globules in the granitic magma, collected in the  
844 cores of the pegmatites after crystallisation of the border zones, and gave rise to the potential B-  
845 Zone and Main-Zone orebodies. Remobilisation of the REE is interpreted to have occurred with  
846 the exsolution of fluids (reduced carbonic and aqueous) prior to or soon after the onset of  
847 pegmatite crystallisation. These early fluids had high salinity and also likely had high pH  
848 (suggested by the precipitation of nahcolite in the Group 3 inclusions). We therefore propose that  
849 the REE were transported initially as hydroxy or hydroxy-fluoride complexes; hydroxy-fluoride  
850 complexes have been shown to be important in the transport of Zr and Nb (Migdisov et al., 2011;  
851 Timofeev et al., 2015).

852 After the system had cooled to ~ 300 °C, there was large-scale production of CO<sub>2</sub> and a sharp  
853 drop in pH (due to the increased activity of dissolved CO<sub>2</sub>). As hydroxy complexes would have  
854 been much less stable under these conditions (there are no data for hydroxy-fluoride complexes),  
855 we speculate that there was a switch to chloride complexation, which is favoured by low pH and  
856 has been shown to be very effective in promoting REE transport (Williams-Jones et al., 2012).

857 Because of the much greater stability of the light REE chloride complexes relative to the heavy  
858 REE complexes (Migdisov and Williams-Jones, 2009), the light REE would have been  
859 preferentially mobilised, which helps explain why the heavy REE are concentrated proximal to  
860 the pegmatites and the light REE have been mobilised for 10s to 100s of metres from them into  
861 the adjacent granite (Gysi et al., 2016). It is also worth noting that the increased activity of  
862 oxidised carbonic species likely led to the precipitation of bastnäsite and its replacement of  
863 primary REE silicates (Vasyukova and Williams-Jones, 2016).

864 In addition to depositing the REE, the increased acidity and relatively low temperature of the  
865 fluid allowed it to alter the sodic zirconsilicate and titanosilicate minerals, e.g., elpidite,  
866 vlasovite, and narsarsukite, replacing them with Ca-bearing equivalents such as gittinsite and  
867 titanite. Aided by further cooling-induced increases in fluoride ion activity, this also caused  
868 significant remobilisation of Zr and Ti as hydroxy-fluoride or hydroxy-chloride complexes  
869 (Rapp et al., 2010; Tanis et al., 2016) and ultimately the dispersion of these metals beyond the  
870 confines of the pegmatites (Gysi et al., 2016).

871 Although the mobilisation of the HREE occurred on a much smaller scale than for the LREE,  
872 evidence for this HREE mobilisation is widespread in the form of secondary gadolinite-group  
873 minerals that occur as concentrically zoned spherules in the granite (locally in association with  
874 hematized arfvedsonite) and display colloform textures in pegmatites (Gysi et al., 2016).  
875 Consistent with the observation that colloform growth is a low temperature phenomenon and  
876 HREE chloride complexes are more stable than LREE chloride complexes at temperatures  $\leq 150$   
877  $^{\circ}\text{C}$  (Migdisov et al., (2009), we therefore propose that the HREE were mobilised late in the  
878 evolution of the hydrothermal system by the highly saline and low temperature Group 5 fluids.

We further propose, given the association of gadolinite-group minerals with hematized arfvedsonite (Reaction 5), that this fluid was also responsible for the widespread hematization that is a feature of the deposit.

## Conclusions

Previously unrecognized early fluid inclusions associated with melt inclusions (Group 1) indicate that hydrothermal activity in the Strange Lake pluton began with the exsolution of a CH<sub>4</sub>-H<sub>2</sub>-bearing aqueous fluid at > 425 °C and 1100 bars that when unmixed contained ~25 wt.% NaCl eq. On cooling, the gas was gradually oxidized to CH<sub>4</sub> + higher hydrocarbons at temperatures between 360 and 325 °C and then to a CO<sub>2</sub>-rich gas at ≤300 °C. The occurrence of common ‘implosion haloes’ around the inclusions indicates that the cooling was isobaric and, based on the intersection of isochores for carbonic and aqueous fluid inclusions, that the pressure was ~1100 bars.

The evolution of the aqueous phase was affected by changes in the gas phase as well as by fluid-rock interaction. Thus, the salinity decreased progressively from ~25 to ~4 wt.% NaCl eq. as a result of alteration of arfvedsonite to aegirine (and hematite). During the final stage of the evolution, fluid salinity increased to the initial level, i.e., ~19 wt.% NaCl eq., due to the reaction of fluid (hydration) with K-feldspar and arfvedsonite to form of Al-, K- and Fe-phyllosilicates. The carbonic component was consumed by fluid-rock interaction when the CO<sub>2</sub>-rich fluid reacted with elpidite, narsarsukite and primary REE-silicates and precipitated nahcolite, bastnäsite-(Ce) and locally interstitial calcite.

899 Our thermodynamic calculations show that the carbonic gas species were in equilibrium at the  
900 time of their entrapment, and changed progressively due to gradual oxidation of the fluid. The C<sub>2</sub>  
901 to C<sub>6</sub> hydrocarbons formed between 360 and 325 °C as a result of oxidative coupling of methane  
902 under conditions of relatively low  $fO_2$  buffered by alteration of arfvedsonite to aegirine.

903 Remobilisation of the LREE occurred relatively early, with the exsolution of a magmatic  
904 hydrothermal fluid that dissolved the REE-rich crystallised fluoride melt and transported the  
905 REE at high pH as hydroxy or hydroxy-fluoride species. When temperature decreased to ~300  
906 °C, there was large-scale oxidation of CH<sub>4</sub> to CO<sub>2</sub>, which strongly increased the activity of  
907 carbonic species in the fluid causing deposition of bastnäsite-(Ce) and also strongly decreased  
908 pH. Consequently there was a switch to chloride complexation of the REE and preferential  
909 mobilisation of the light REE on a scale of 10s to 100s of metres. The accompanying increase in  
910 acidity, and relatively low temperature of this fluid also allowed it to alter the sodic zirconsilicate  
911 and titanosilicate minerals, e.g., elpidite, vlasovite, and narsarsukite, replacing them with Ca-  
912 bearing equivalents, such as gittinsite and titanite. Aided by further cooling-induced increases in  
913 fluoride ion activity, this led to significant remobilisation of Zr and Ti and ultimately the  
914 dispersion of these metals beyond the confines of the pegmatites. Hydrothermal activity  
915 terminated with local remobilisation of the HREE by a low temperature high salinity fluid that  
916 likely was also responsible for the intense hematization of arfvedsonite that characterises some of  
917 the best mineralised parts of the deposit.

## 918    **Acknowledgments**

919    The research was funded by Discovery and Collaborative Research and Development grants  
920    (Quest Rare Minerals Ltd.) from NSERC (Canada), and a team grant from FQRNT (Québec).  
921    Peter Cashin, President of Quest Rare Minerals and exploration team members, P. Guay and P.  
922    Collins provided essential logistical support and valuable advice on the geology of the B-Zone  
923    deposit at Strange Lake. Alex Gysi provided B-Zone Samples SL-11-14 to SL-11-45. The  
924    manuscript was improved significantly by the constructive reviews of R. Thomas and I. Samson.

## 925    **References**

- 926    Bakker, R.J., 1999. Adaptation of the Bowers and Helgeson (1983) equation of state to the H<sub>2</sub>O-  
927    CO<sub>2</sub>-CH<sub>4</sub>-N<sub>2</sub>-NaCl system. *Chemical Geology* 154, 225-236.
- 928    Bakker, R.J., 2003. Package FLUIDS 1. Computer programs for analysis of fluid inclusion data  
929    and for modelling bulk fluid properties. *Chemical Geology* 194, 3-23.
- 930    Bakker, R.J., Jansen, J.B., 1994. A Mechanism for preferential H<sub>2</sub>O leakage from fluid  
931    inclusions in quartz, based on TEM observations. *Contrib Mineral Petr* 116, 7-20.
- 932    Balitskaya, O.V., Balitsky, V.S., 2010. Mechanisms of the Formation and Morphogenetic Types  
933    of Fluid Inclusions in Crystals of Synthetic Minerals. *Dokl Earth Sci* 435, 1442-1445.
- 934    Balitsky, V.S., Prokof'ev, V.Y., Balitskaya, L.V., Bublikova, T.M., Pentelei, S.V., 2007.  
935    Experimental study of the interaction of mineral-forming hydrothermal solutions with oil and  
936    their joint migration. *Petrology+* 15, 211-223.
- 937    Blamey, N.J.F., 2012. Composition and evolution of crustal, geothermal and hydrothermal fluids  
938    interpreted using quantitative fluid inclusion gas analysis. *J Geochem Explor* 116, 17-27.
- 939    Blamey, N.J.F., Parnell, J., McMahon, S., Mark, D.F., Tomkinson, T., Lee, M., Shivak, J.,  
940    Izawa, M.R.M., Banerjee, N.R., Flemming, R.L., 2015. Evidence for methane in Martian  
941    meteorites. *Nat Commun* 6.

- 942 Boily, M., Williams-Jones, A.E., 1994. The role of magmatic and hydrothermal processes in the  
943 chemical evolution of the Strange Lake plutonic complex, Quebec-Labrador. *Contrib Mineral*  
944 *Petr* 118, 33-47.
- 945 Braitsch, O., 1964. The temperature of evaporite formation, in: Nairn, A.E.M. (Ed.), *Problems in*  
946 *palaeoclimatology*. Wiley, New York, pp. 479-490.
- 947 Burke, E.A.J., 2001. Raman microspectrometry of fluid inclusions. *Lithos* 55, 139-158.
- 948 Chao, J., Wilhoit, R.C., Zwolinski, B.J., 1973. Ideal gas thermodynamic properties of ethane and  
949 propane. *J. Phys. Chem. Ref. Data* 2, 427-438.
- 950 CODATA, 1978. CODATA recommended key values for thermodynamics 1977. *The Journal of*  
951 *Chemical Thermodynamics* 10, 903-906.
- 952 Duan, Z.H., Moller, N., Weare, J.H., 1992a. An equation of state for the CH<sub>4</sub>-CO<sub>2</sub>-H<sub>2</sub>O System  
953 .1. Pure systems from 0-Degrees-C to 1000-Degrees-C and 0 to 8000 Bar. *Geochimica Et*  
954 *Cosmochimica Acta* 56, 2605-2617.
- 955 Duan, Z.H., Moller, N., Weare, J.H., 1992b. An equation of state for the CH<sub>4</sub>-CO<sub>2</sub>-H<sub>2</sub>O system  
956 .2. Mixtures from 50-Degrees-C to 1000-Degrees-C and 0 to 1000 Bar. *Geochimica Et*  
957 *Cosmochimica Acta* 56, 2619-2631.
- 958 Duan, Z.H., Moller, N., Weare, J.H., 1996. A general equation of state for supercritical fluid  
959 mixtures and molecular dynamics simulation of mixture PVTX properties. *Geochimica Et*  
960 *Cosmochimica Acta* 60, 1209-1216.
- 961 Ernst, W.G., 1962. Synthesis, Stability Relations, and Occurrence of Riebeckite and Riebeckite-  
962 Arfvedsonite Solid Solutions. *Journal of Geology* 70, 689-736.
- 963 Evans, B.W., 2007. The synthesis and stability of some end-member amphiboles. *Amphiboles:*  
964 *Crystal Chemistry, Occurrence, and Health Issues* 67, 261-286.
- 965 Frezzotti, M.L., Tecce, F., Casagli, A., 2012. Raman spectroscopy for fluid inclusion analysis. *J*  
966 *Geochem Explor* 112, 1-20.
- 967 Goldstein, R.H., 2001. Fluid inclusions in sedimentary and diagenetic systems. *Lithos* 55, 159-  
968 193.
- 969 Götze, J., 2009. Chemistry, textures and physical properties of quartz - geological interpretation  
970 and technical application. *Mineralogical Magazine* 73, 645-671.
- 971 Gysi, A.P., Williams-Jones, A.E., 2013. Hydrothermal mobilization of pegmatite-hosted REE  
972 and Zr at Strange Lake, Canada: A reaction path model. *Geochimica et Cosmochimica Acta* 122,  
973 324-352.

- 974 Gysi, A.P., Williams-Jones, A.E., Collins, P., 2016. Lithogeochemical Vectors for Hydrothermal  
975 Processes in the Strange Lake Peralkaline Granitic REE-Zr-Nb Deposit. *Econ Geol* 111, 1241-  
976 1276.
- 977 Holloway, J.R., 1984. Graphite-CH<sub>4</sub>-H<sub>2</sub>O-CO<sub>2</sub> equilibria at low-grade metamorphic conditions.  
978 *Geology* 12, 455-458.
- 979 Marion, G.M., 2001. Carbonate mineral solubility at low temperatures in the Na-K-Mg-Ca-H-Cl-  
980 SO<sub>4</sub>-OH-HCO<sub>3</sub>-CO<sub>3</sub>-CO<sub>2</sub>-H<sub>2</sub>O system. *Geochimica et Cosmochimica Acta* 65, 1883-1896.
- 981 Migdisov, A.A., Williams-Jones, A.E., 2009. The stability of Zr in F-bearing hydrothermal  
982 solutions. *Geochimica Et Cosmochimica Acta* 73, A879-A879.
- 983 Migdisov, A.A., Williams-Jones, A.E., van Hinsberg, V., Salvi, S., 2011. An experimental study  
984 of the solubility of baddeleyite (ZrO<sub>2</sub>) in fluoride-bearing solutions at elevated temperature.  
985 *Geochimica Et Cosmochimica Acta* 75, 7426-7434.
- 986 Migdisov, A.A., Williams-Jones, A.E., Wagner, T., 2009. An experimental study of the  
987 solubility and speciation of the Rare Earth Elements (III) in fluoride- and chloride-bearing  
988 aqueous solutions at temperatures up to 300 degrees C. *Geochimica Et Cosmochimica Acta* 73,  
989 7087-7109.
- 990 Miller, R.R., Heaman, L.M., Birkett, T.C., 1997. U-Pb zircon age of the Strange Lake  
991 peralkaline complex: Implications for Mesoproterozoic peralkaline magmatism in north-central  
992 Labrador. *Precambrian Res* 81, 67-82.
- 993 Nassif, J.G., 1993. The Strange Lake peralkaline complex, Quebec-Labrador: The hypersolvus-  
994 subsolvus granite transition and feldspar mineralogy. McGill University, Montreal, p. 104.
- 995 Rapp, J.F., Klemme, S., Butler, I.B., Harley, S.L., 2010. Extremely high solubility of rutile in  
996 chloride and fluoride-bearing metamorphic fluids: An experimental investigation. *Geology* 38,  
997 323-326.
- 998 Reid, R.C., Prausnitz, J.M., Poling, B.E., 1987. The properties of gases and liquids. McGraw Hill  
999 Book Co., New York, NY.
- 1000 Robie, A., Hemingway, B.S., 1995. Thermodynamic properties of minerals and related  
1001 substances at 298.15 K and 1 bar (10<sup>5</sup> pascals) pressure and at higher temperatures. U.S.  
1002 geological survey bulletin 2131, Washington.
- 1003 Robie, A., Hemingway, B.S., Fisher, J.R., 1978. Thermodynamic properties of minerals and  
1004 related substances at 298.15 K and 1 bar (10<sup>5</sup> pascals) pressure and at higher temperatures. U.S.  
1005 geological survey bulletin 1452, Washington.

- 1006 Salvi, S., Williams-Jones, A.E., 1990. The role of hydrothermal processes in the granite-hosted  
1007 Zr, Y, Re deposit at Strange Lake, Quebec Labrador - evidence from fluid inclusions.  
1008 *Geochimica Et Cosmochimica Acta* 54, 2403-2418.
- 1009 Salvi, S., Williams-Jones, A.E., 1992. Reduced Orthomagmatic C-O-H-N-NaCl Fluids in the  
1010 Strange Lake Rare-Metal Granitic Complex, Quebec Labrador, Canada. *Eur J Mineral* 4, 1155-  
1011 1174.
- 1012 Salvi, S., Williams-Jones, A.E., 1996. The role of hydrothermal processes in concentrating high-  
1013 field strength elements in the Strange Lake peralkaline complex, northeastern Canada.  
1014 *Geochimica Et Cosmochimica Acta* 60, 1917-1932.
- 1015 Salvi, S., Williams-Jones, A.E., 1997. Fischer-Tropsch synthesis of hydrocarbons during sub-  
1016 solidus alteration of the Strange Lake peralkaline granite, Quebec/Labrador, Canada.  
1017 *Geochimica Et Cosmochimica Acta* 61, 83-99.
- 1018 Salvi, S., Williams-Jones, A.E., 2006. Alteration, HFSE mineralisation and hydrocarbon  
1019 formation in peralkaline igneous systems: Insights from the Strange Lake Pluton, Canada. *Lithos*  
1020 91, 19-34.
- 1021 Shvarov, Y.V., 1999. Algorithmization of the numeric equilibrium modeling of dynamic  
1022 geochemical processes. *Geokhimiya+*, 646-652.
- 1023 Shvarov, Y.V., Bastrakov, E.N., 1999. HCh: a software package for geochemical equilibrium  
1024 modelling. User's Guide. Australian Geological Survey Organisation, Record 1999/25.
- 1025 Sterner, S.M., Bodnar, R.J., 1989. Synthetic fluid inclusions VII. Re-equilibration of fluid  
1026 inclusions in quartz during laboratory-simulated metamorphic burial and uplift. *Journal of*  
1027 *Metamorphic Geology* 7, 243-260.
- 1028 Stryjek, R., Vera, J.H., 1986. PRSV - an improved Peng-Robinson equation of state for pure  
1029 compounds and mixtures. *Can J Chem Eng* 64, 323-333.
- 1030 Stull, D.R., Westrum, E.F., Sinke, G.C., 1969. The chemical thermodynamics of organic  
1031 compounds. New York, J. Wiley.
- 1032 Tanis, E.A., Simon, A., Zhang, Y.X., Chow, P., Xiao, Y.M., Hanchar, J.M., Tschauner, O., Shen,  
1033 G.Y., 2016. Rutile solubility in NaF-NaCl-KCl-bearing aqueous fluids at 0.5-2.79 GPa and 250-  
1034 650 degrees C. *Geochimica Et Cosmochimica Acta* 177, 170-181.
- 1035 Timofeev, A., Migdisov, A.A., Williams-Jones, A.E., 2015. An experimental study of the  
1036 solubility and speciation of niobium in fluoride-bearing aqueous solutions at elevated  
1037 temperature. *Geochimica Et Cosmochimica Acta* 158, 103-111.



- 1038 Vasyukova, O.V., Fonarev, V.I., 2006. Experimental modeling of the transformation of H<sub>2</sub>O-  
1039 CO<sub>2</sub>-CH<sub>4</sub> inclusions during isobaric cooling and isothermal compression. *Geochem Int+* 44,  
1040 1170-1180.
- 1041 Vasyukova, O.V., Williams-Jones, A.E., 2014. Fluoride–silicate melt immiscibility and its role  
1042 in REE ore formation: Evidence from the Strange Lake rare metal deposit, Quebec-Labrador,  
1043 Canada. *Geochimica et Cosmochimica Acta* 139, 110-130.
- 1044 Vasyukova, O.V., Williams-Jones, A.E., 2016. The evolution of immiscible silicate and fluoride  
1045 melts: implications for REE ore-genesis. *Geochimica et Cosmochimica Acta* 172, 205-224.
- 1046 Vityk, M.O., Bodnar, R.J., 1995. Textural evolution of synthetic fluid inclusions in quartz during  
1047 reequilibration, with applications to tectonic reconstruction. *Contrib Mineral Petr* 121, 309-323.
- 1048 Vityk, M.O., Bodnar, R.J., Doukhan, J.C., 2000. Synthetic fluid inclusions. XV. TEM  
1049 investigation of plastic flow associated with reequilibration of fluid inclusions in natural quartz.  
1050 *Contrib Mineral Petr* 139, 285-297.
- 1051 Vityk, M.O., Bodnar, R.J., Dudok, I.V., 1995. Natural and synthetic re-equilibration textures of  
1052 fluid inclusions in quartz (Marmarosh diamonds) - evidence for refilling under conditions of  
1053 compressive loading. *Eur J Mineral* 7, 1071-1087.
- 1054 Williams-Jones, A.E., Migdisov, A.A., Samson, I.M., 2012. Hydrothermal mobilisation of the  
1055 rare earth elements - a tale of "Ceria" and "Yttria". *Elements* 8, 355-360.
- 1056 Zajac, I.S., Miller, R.R., Birkett, T.C., Nantel, S., 1984. Le gîte de Zr, Y, Nb, and Be du  
1057 complexe alcalin de Strange Lake, Québec-Labdrador, in: *Ressources, M.d.l.É.e.d. (Ed.)*,  
1058 Québec, pp. 127-142.

1059

## 1060 **Figure captions**

1061 Figure 1. A geological map of the Strange Lake pluton showing the distribution of the principal  
1062 rock types and the locations of the samples on which this study was based. The map was  
1063 provided by Quest Rare Minerals Ltd.

1064 Figure 2. Photomicrographs of Groups 1 and 2 fluid inclusions. (a) and (b) – Group 1 fluid  
1065 inclusions trapped together with melt inclusions (large, dark and irregularly-shaped) as an

1066 isolated group (a) and along a growth zone (b). (c) – an enlargement of the area identified as (c)  
1067 in (b). (d) – Healed fracture with Group 2a inclusions that crosscut a growth zone containing  
1068 Group 1 inclusions. Insets in (c) and (d) show areas within a quartz grain from Sample 204722;  
1069 the black dashed lines represent growth zones containing Group 1 inclusions and the blue dashed  
1070 line a healed fracture containing Group 2a inclusions. The inset in (b) shows the Raman  
1071 spectrum for a Group 1 inclusion.

1072 Figure 3. Histograms showing the salinity of the aqueous phase in the different inclusion Groups.  
1073 Group 3\* represents Type V inclusions in Group 3 for which salinity was determined from the  
1074 temperature of clathrate melting.

1075 Figure 4. Photomicrographs of Group 2 inclusions (CH<sub>4</sub>-rich) and their Raman spectra. (a) and  
1076 (b) – Primary Group 2a inclusions in Sample 16. (c) – Primary Group 2b inclusions, Sample 13.  
1077 (d) – Secondary Group 2b inclusions, Sample 13. (e) – Raman spectra for typical Group 2a  
1078 (blue) and Group 2b (red) inclusions. Type II – carbonic, Type IV – aqueous and Type V –  
1079 mixed aqueous-carbonic inclusions.

1080 Figure 5. Histograms showing homogenisation temperatures for Type II inclusions: (a) – Group  
1081 2a (pink) and 2b (blue) inclusions. (b) – Group 3 inclusions, grey – Sample 11, orange – Sample  
1082 SL-11-45, purple – Sample SL-11-43 and yellow – Sample 2. \* - data for these plots are from  
1083 individual inclusions (not FIAs).

1084 Figure 6. Effects of cooling on Group 3 fluid inclusions (Sample 11). (a) – A general view  
1085 showing a random 3D distribution of the inclusions, which indicates their primary origin. (b),  
1086 (d), (f), (h) – inclusions before cooling that are illustrated in (a) and located by rectangles labeled

1087 with the corresponding letters; (j) also shows an inclusion before cooling. (c), (e), (g), (i) and (k)  
1088 – inclusions (b), (d), (f), (h) and (j) after cooling. (b), (c) – Type IV inclusions, the upper left  
1089 inclusion decrepitated upon cooling. (d), (e) – Type VI-2 inclusion, nahcolite crystallised after  
1090 cooling. (f), (g) – Type V inclusion, no change after cooling. (h), (i) – Type VI-1 inclusion with  
1091 nahcolite crystal, the volume of nahcolite increased after cooling. Inset in (h) – microphotograph  
1092 made in crossed polars to show the high birefringence of the nahcolite crystal. (j) and (k) - Type  
1093 VI-2 inclusion with a very pronounced ‘implosion’ halo, nahcolite crystallised on cooling.

1094 Figure 7. Distribution of Group 3 and 4 inclusions in Sample SL-11-45. (a) – a sketch illustrating  
1095 the distribution of the Group 3 inclusions in growth zones (black dashed lines) that are crosscut  
1096 by two fractures containing Group 4 inclusions (two blue dashed lines) and late healed  
1097 dislocations (red lines). (b) to (e) – microphotographs of rectangular areas in (a) labeled with the  
1098 corresponding letters. (b) – an overview and enlarged images of selected secondary Group 4  
1099 inclusions. (c) – an overview and enlarged images of selected primary Type VI-2 inclusions.  
1100 Note that the photographs were made after freezing cycles and, as a result, the inclusions contain  
1101 fine-grained aggregates of nahcolite (Nah). (d) – an overview and enlarged images of the area in  
1102 which primary Type VI-2 inclusions are crosscut by late healed dislocations. (e) – an overview  
1103 and enlarged images of growth zones with Type V inclusions.

1104 Figure 8. Representative Raman spectra for the different types of Group 3 inclusions. (a) – gas-  
1105 rich Type II inclusions, (b) – aqueous Type IV inclusions, (c) – Type VI-1 inclusions and (d) –  
1106 Type VI-2 inclusions (blue spectrum – nahcolite, red spectrum – gas bubble).

1107 Figure 9. Group 4 and 5 fluid inclusions. (a) – Group 5a inclusions defining the edges of a  
1108 pseudomorph (Sample 204739). (b), (c) – Primary Group 5b inclusions in the latest quartz  
1109 generation (sample 204739): overview (b) and magnified image showing inclusions containing  
1110 anhedral albite crystals (c). (d) – primary Group 4 inclusions forming 3D arrays and secondary  
1111 Group 5c inclusions extending from a pseudomorph (Sample SL-11-14).

1112 Figure 10. A schematic pH-T path for Strange Lake fluid, constrained by the compositions of  
1113 Group 3 fluid inclusions.

1114 Figure 11. The calculated pressure-temperature path for the evolving fluids at Strange Lake. The  
1115 numbers 1 – 5 indicate the entrapment pressure and temperature for Group 1 (1), Group 2a (2),  
1116 Group 2b (3), Group 4 (4) and Group 5 (5) inclusions. The number 6 refers to an estimate made  
1117 for CO<sub>2</sub>-rich inclusions (Type V) in sample SL-11-45. The letters a to g refer to isochores for  
1118 selected inclusions, the properties of which are reported in Table 4.

1119 Figure 12. The calculated log  $f_{O_2}$ -T path for the evolution of the Strange Lake fluids (see the  
1120 main text for details of the calculations) compared to those of selected oxygen fugacity buffers,  
1121 and fluid paths (path 1 and path 2) proposed by Gysi and Williams-Jones (2013). Note that point  
1122 4 represents the  $f_{O_2}$  of a fluid that would have been in equilibrium with the Group 4 fluid had  
1123 that fluid contained CO<sub>2</sub>.

Figure1

[Click here to download high resolution image](#)

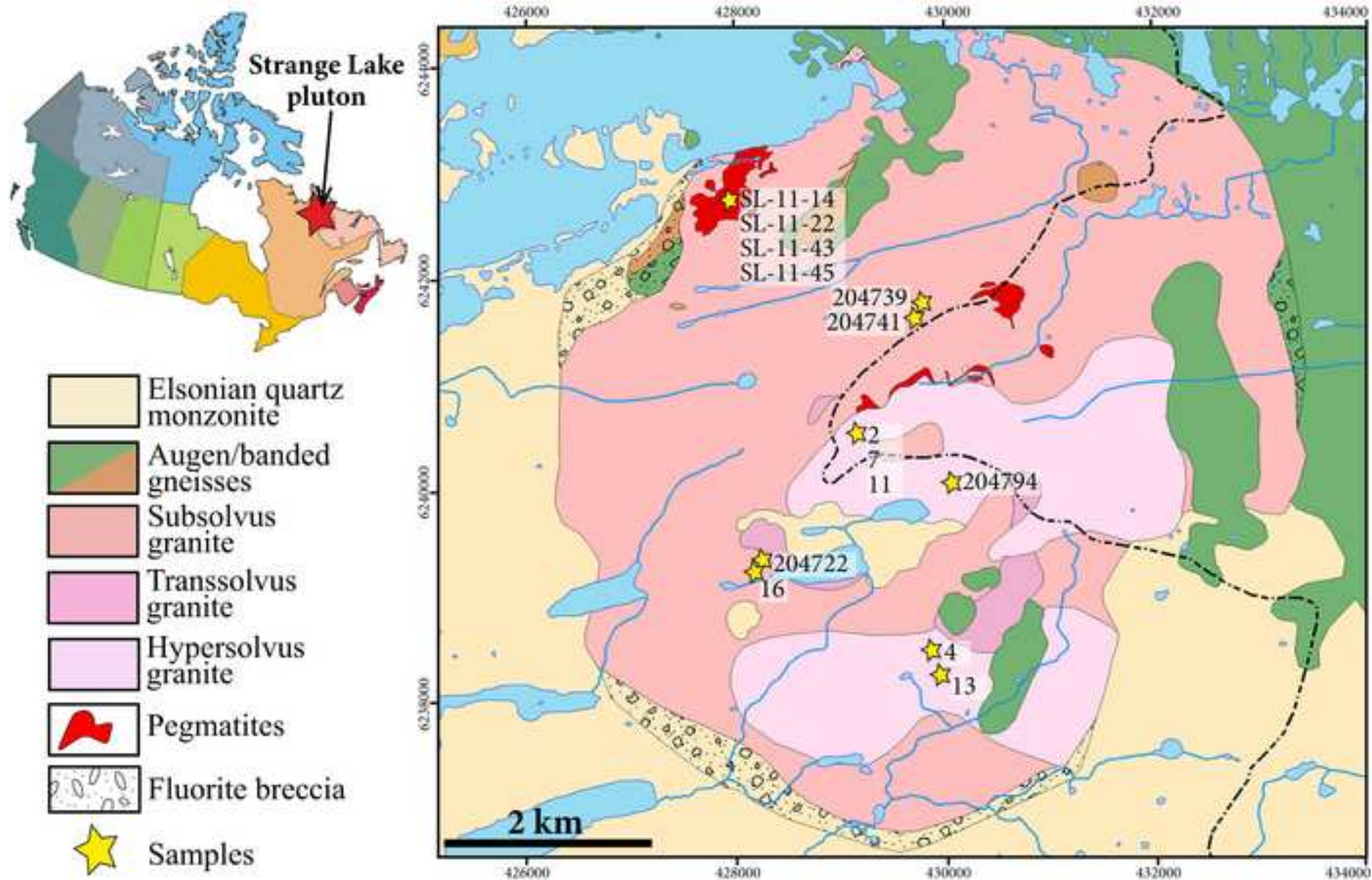




Figure2

[Click here to download high resolution image](#)

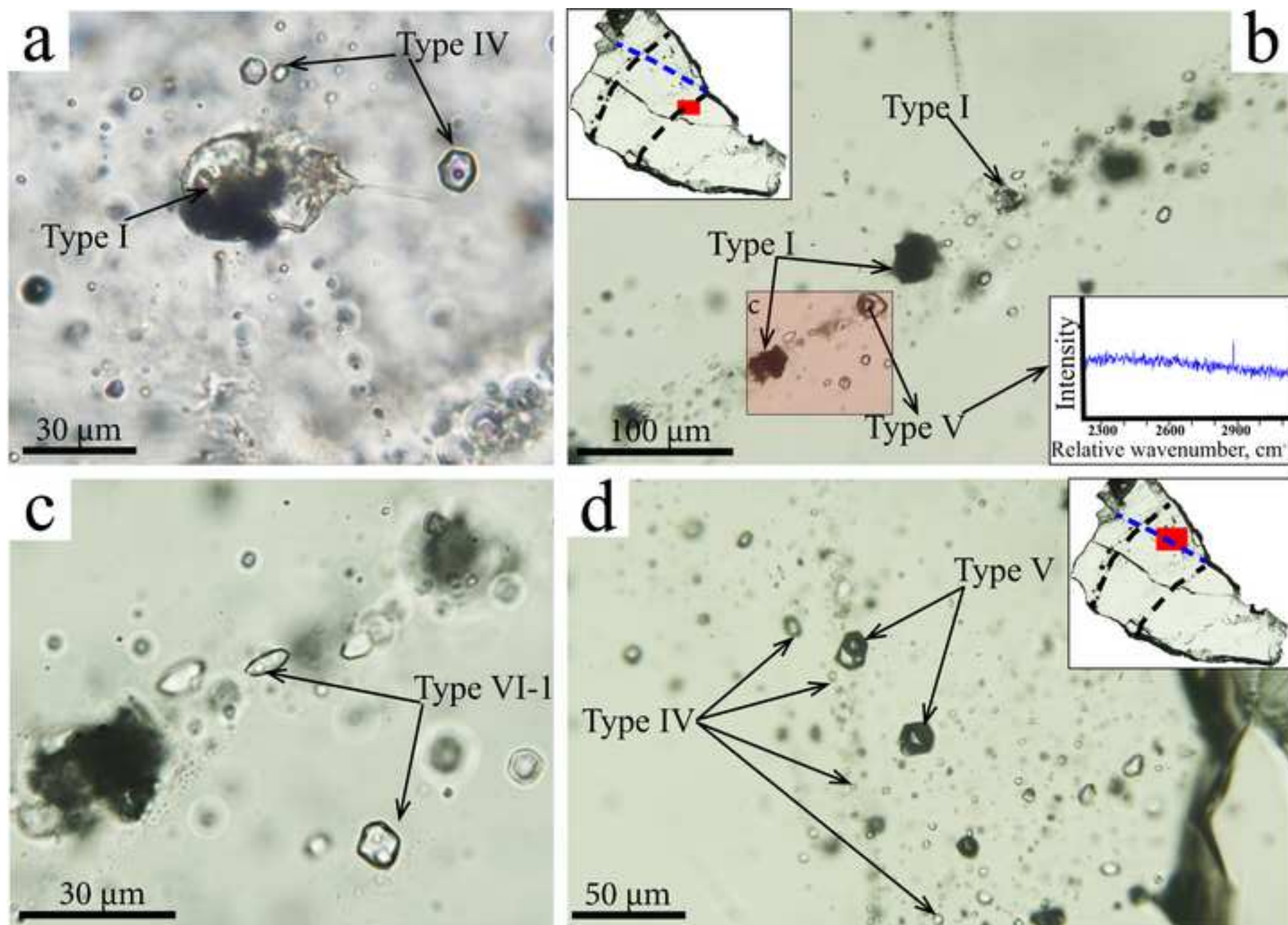


Figure3  
[Click here to download high resolution image](#)

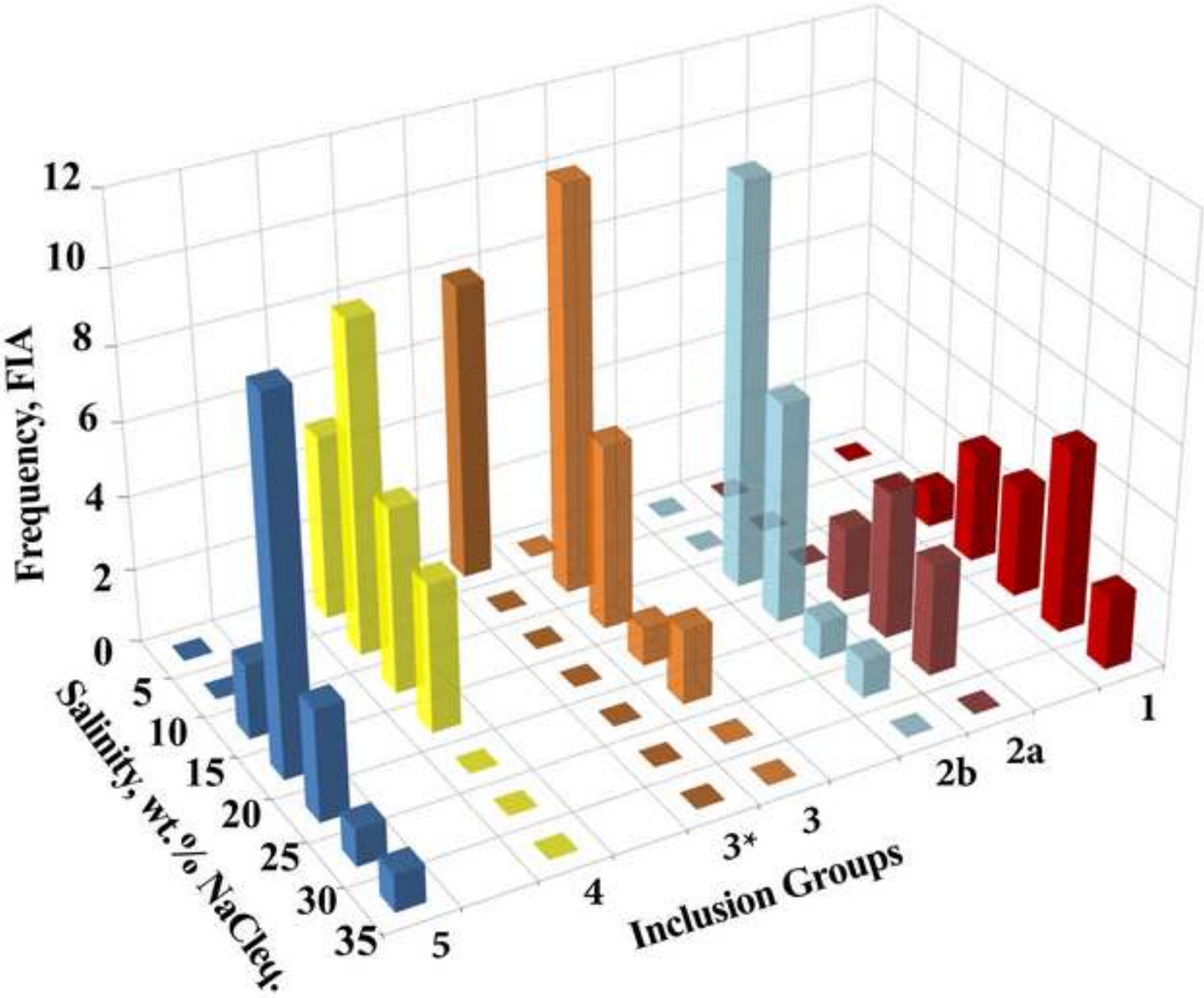


Figure4

[Click here to download high resolution image](#)

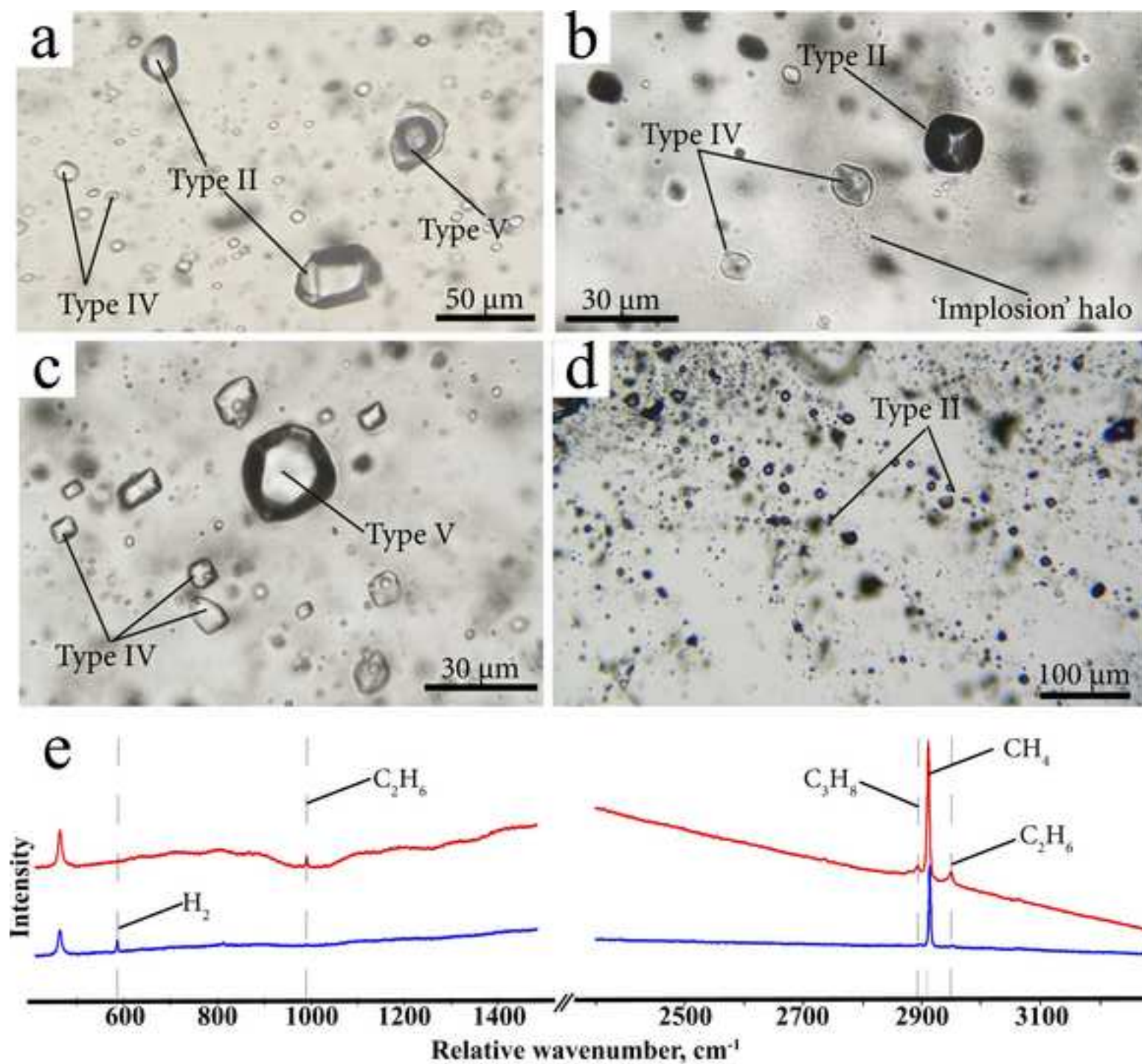
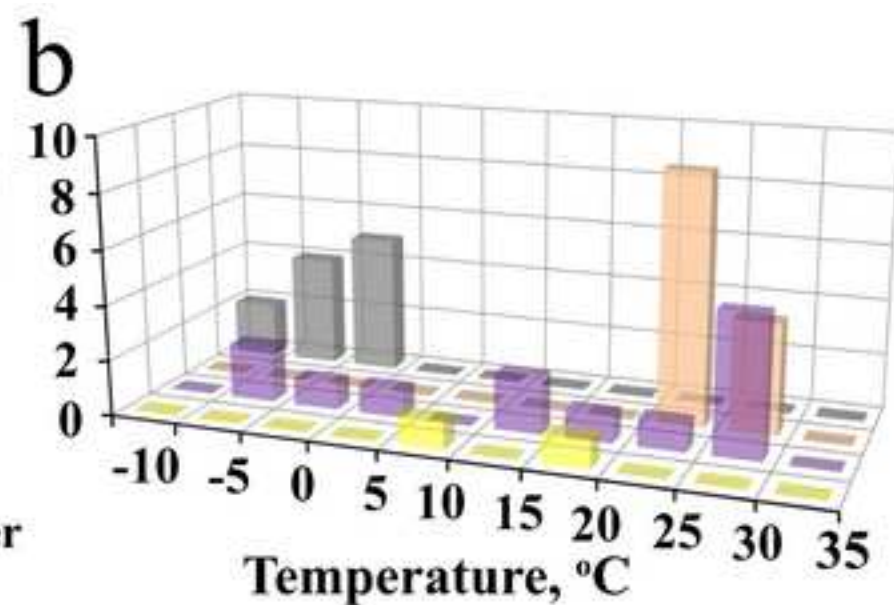
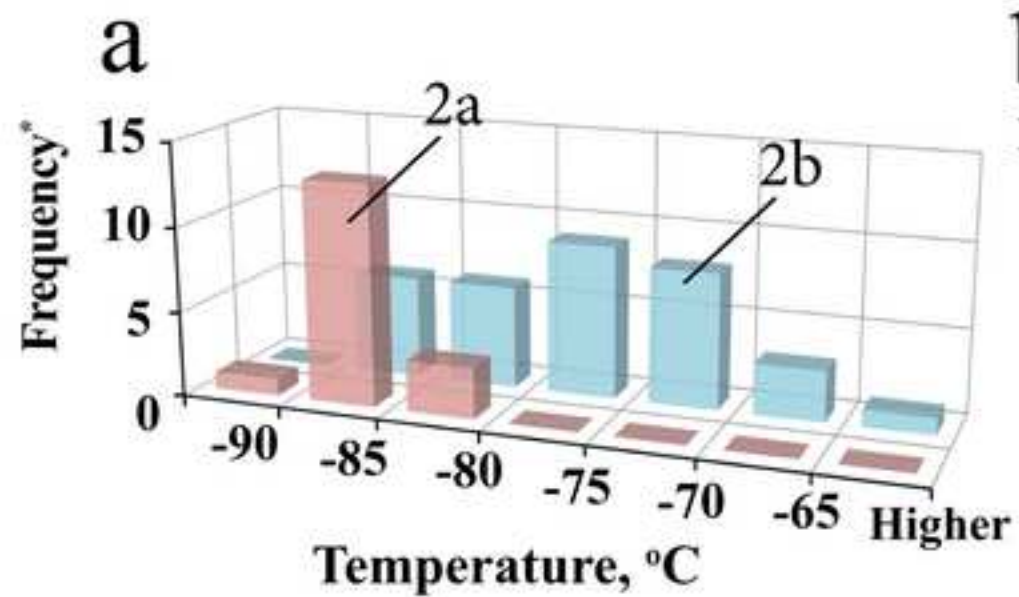




Figure5

[Click here to download high resolution image](#)



**Figure6**  
[Click here to download high resolution image](#)

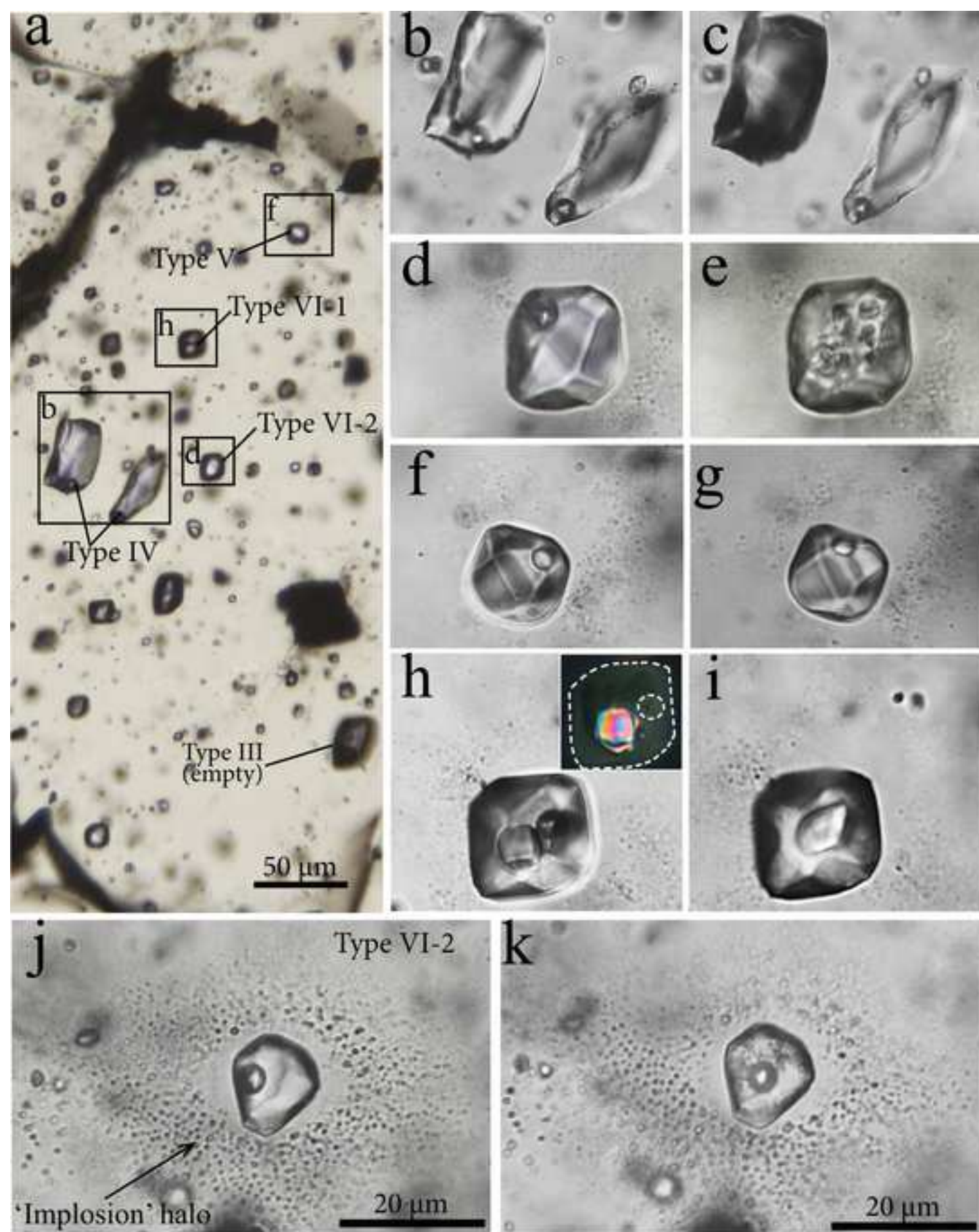




Figure7  
[Click here to download high resolution image](#)

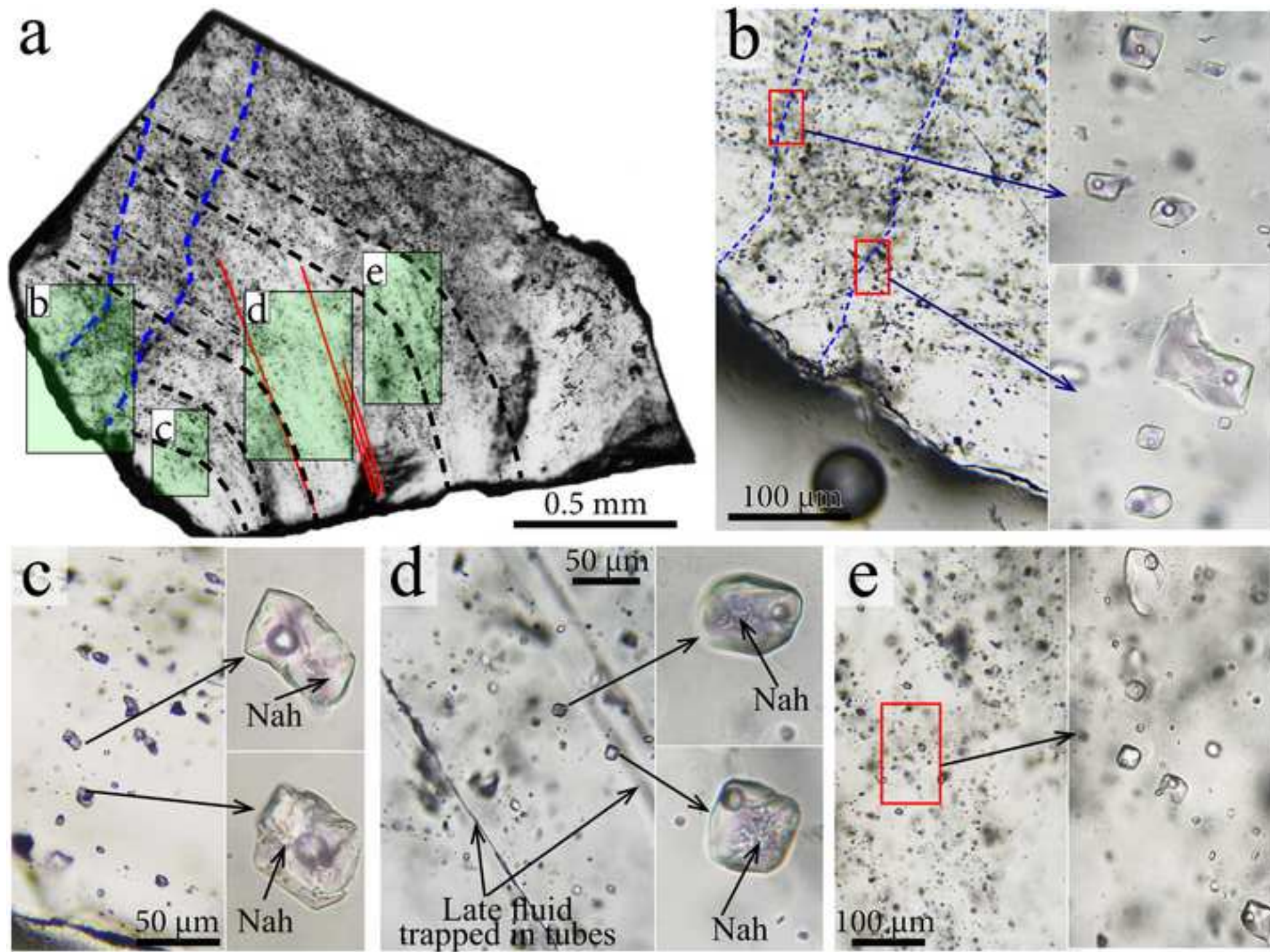


Figure8

[Click here to download high resolution image](#)

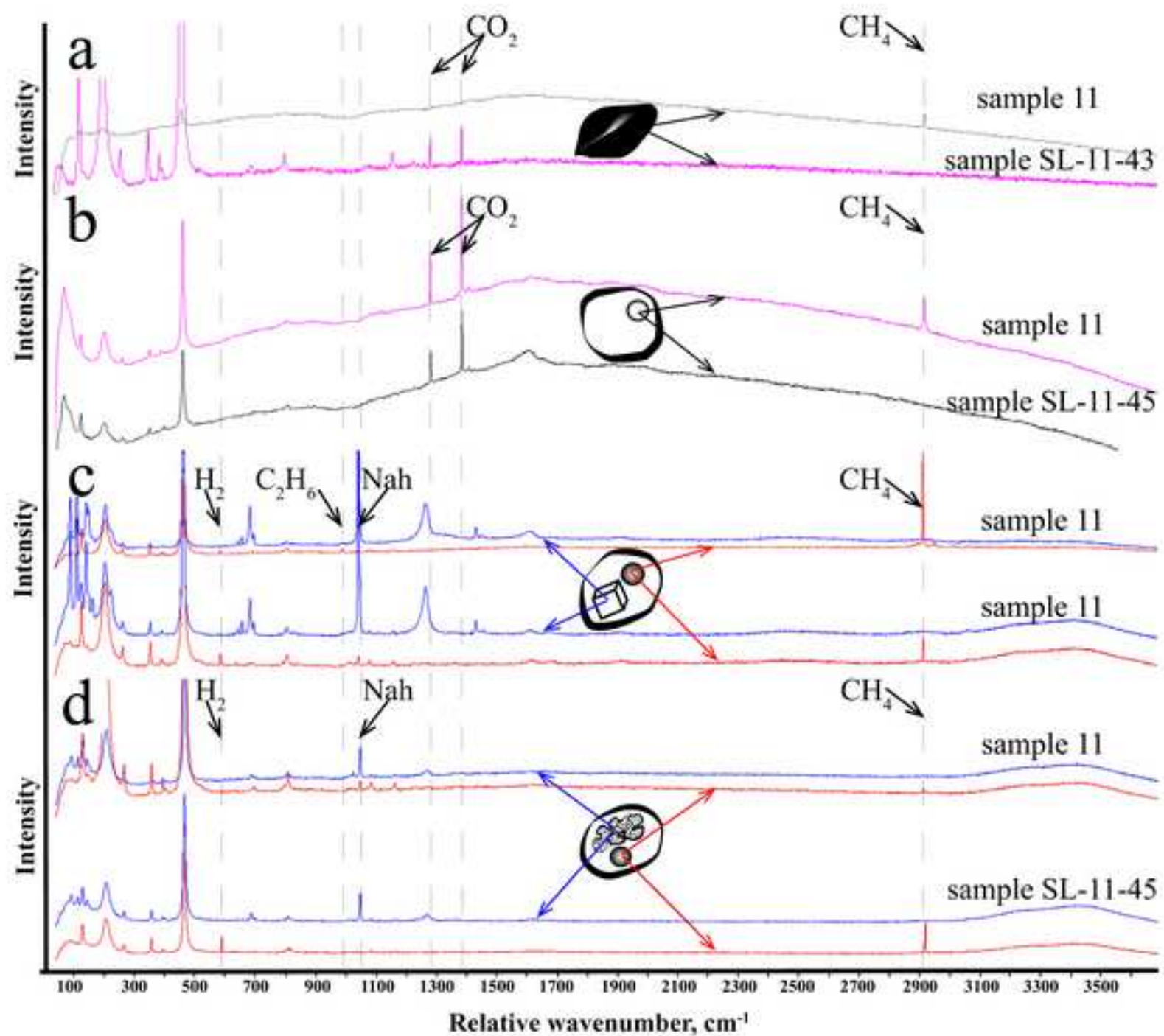




Figure9  
[Click here to download high resolution image](#)

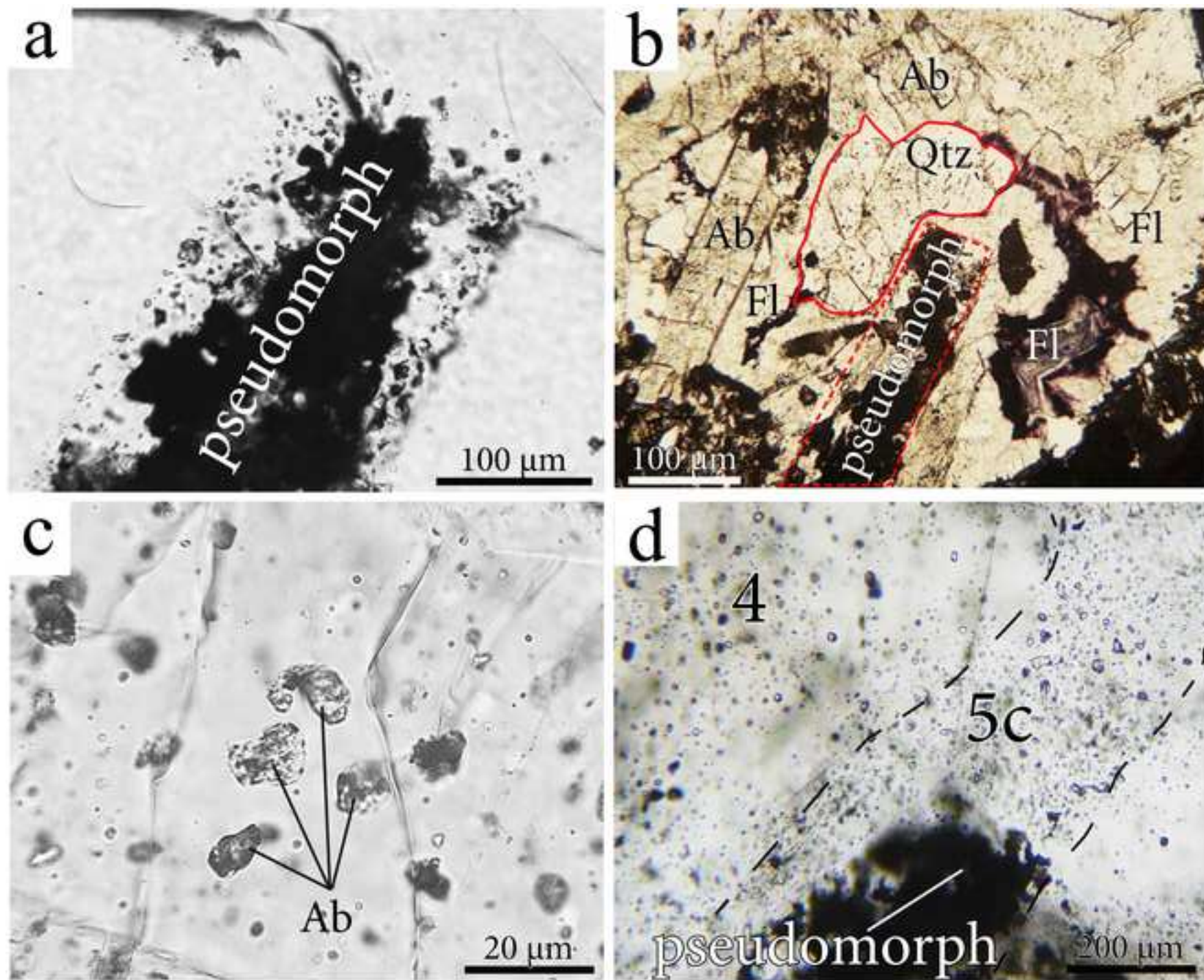


Figure10  
[Click here to download high resolution image](#)

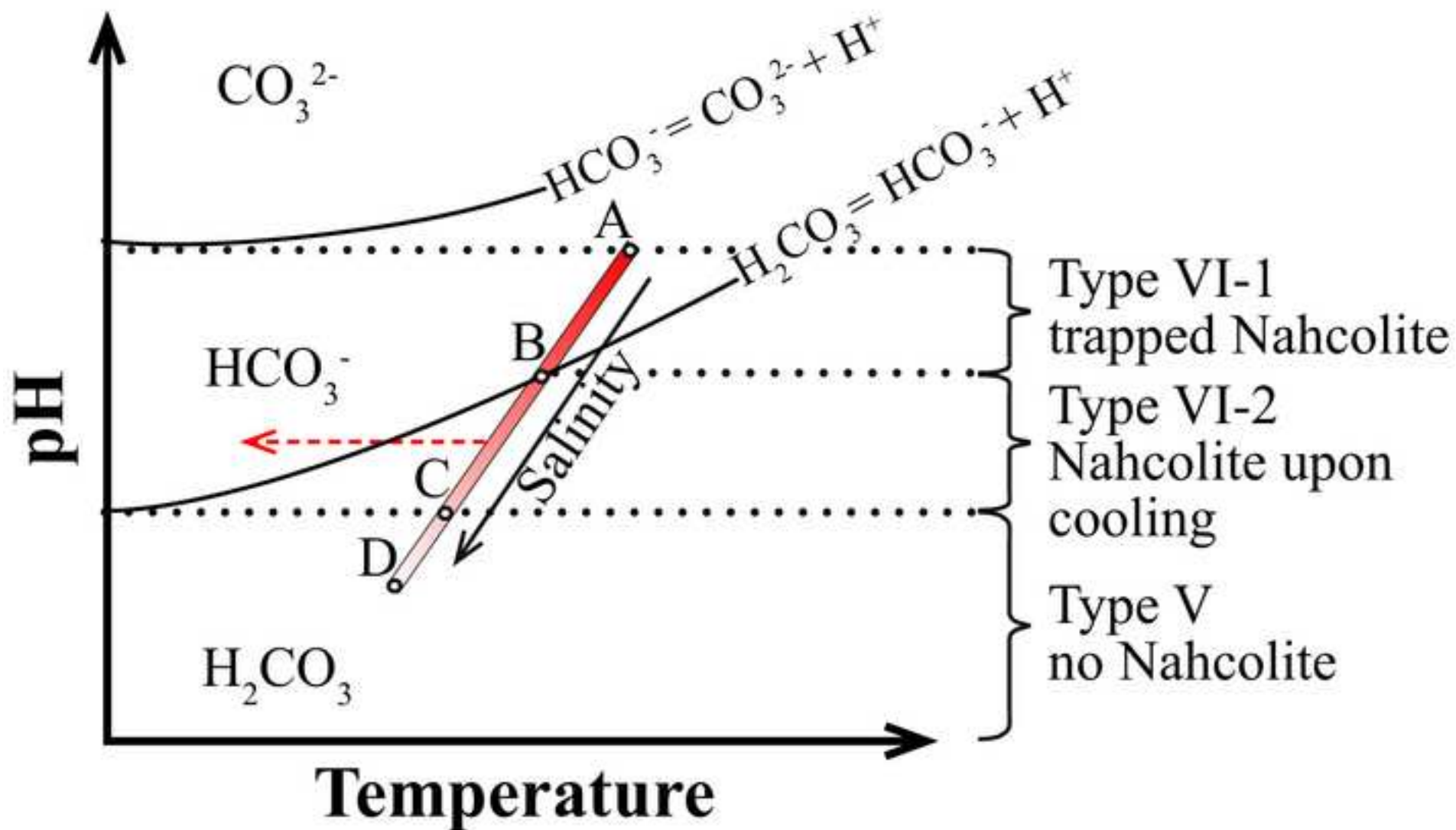


Figure11  
[Click here to download high resolution image](#)

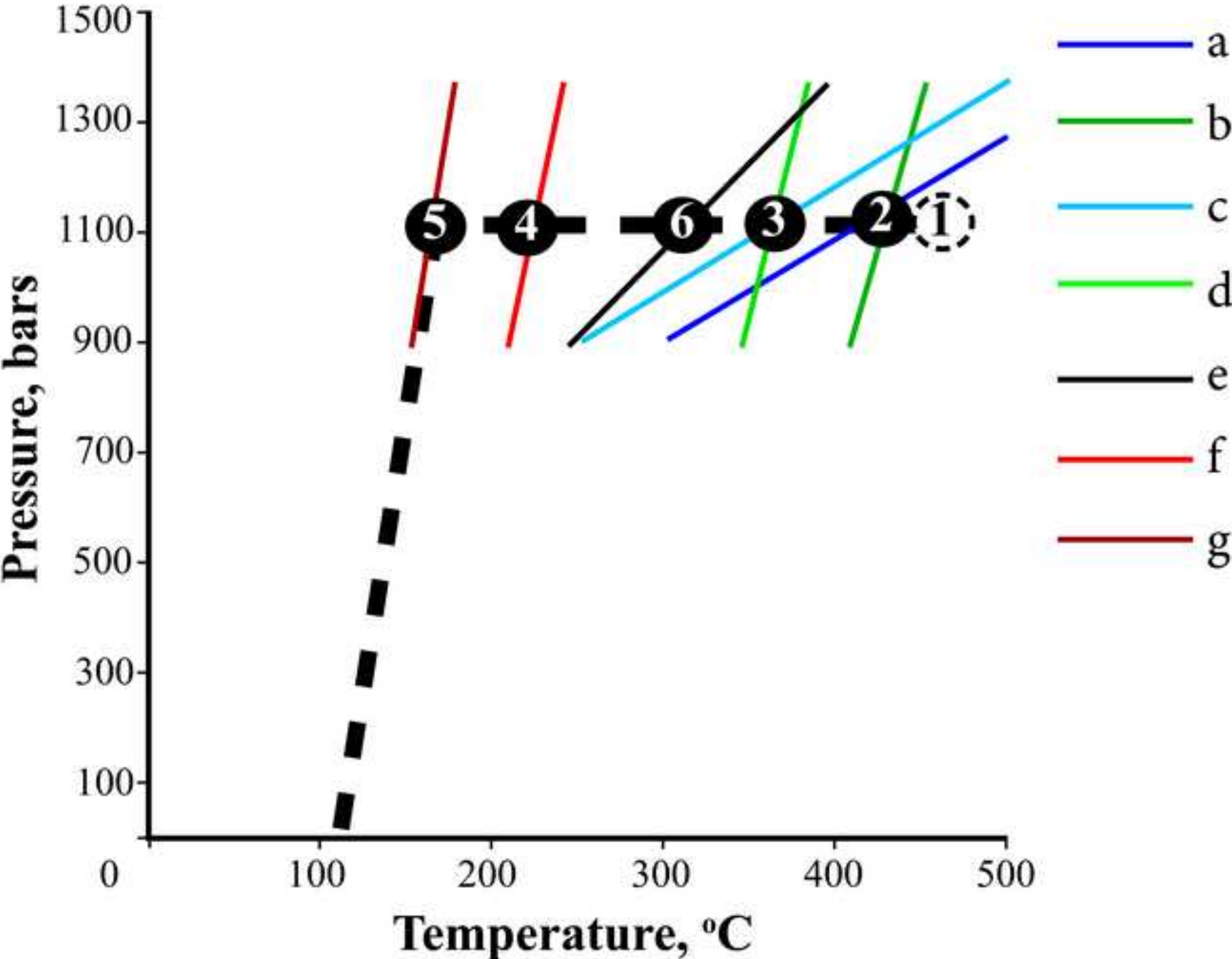




Figure12  
[Click here to download high resolution image](#)

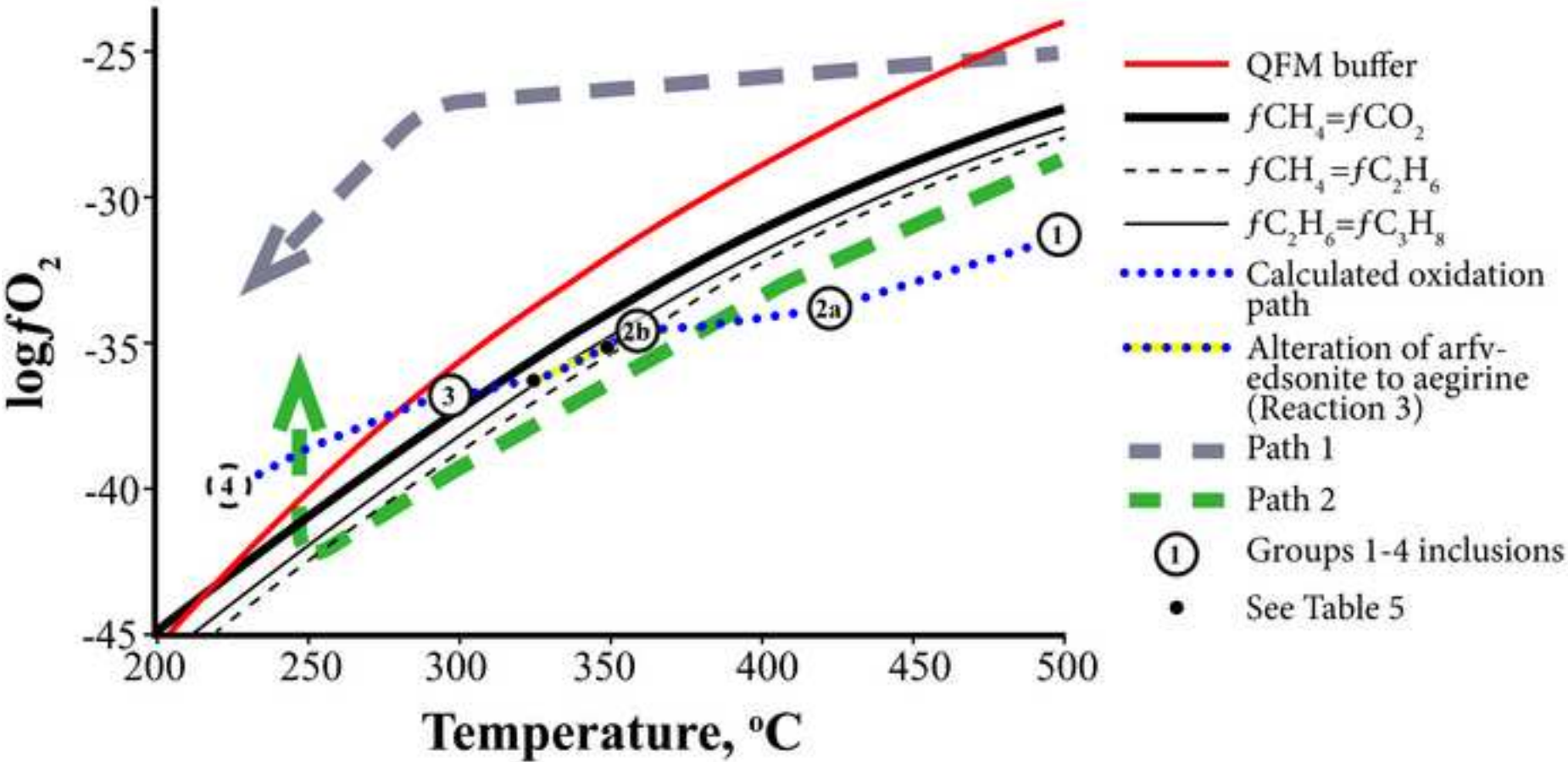








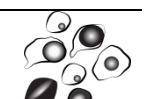

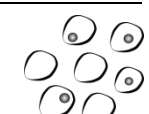
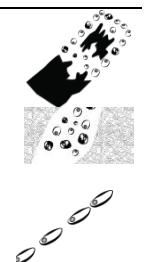




Table 1 Sample descriptions

Sample N	Type of sample	Sample type	Alteration	Mineralogy	Major inclusion Groups present	Methods applied	
						Microthermometry	Bulk gas analysis
2	Drill core	Vein	Altered	Massive quartz	3	■	■
4	Outcrop	Border pegmatite	Unaltered	Large crystals of quartz, K-feldspar and arfvedsonite	1	-	■
7	Drill core	Pegmatite core	Altered	Massive quartz, hematized along fractures	4 and 5	■	■
11	Drill core	Pegmatite core	Altered	Massive quartz	3	■	■
13	Outcrop	Pegmatite core	Partially altered	Massive quartz	2b	■	■
204722	Outcrop	Layered border pegmatite	Unaltered	Layers of quartz, K-feldspar and arfvedsonite	1 (minor 2a)	■	■
16	Outcrop	Border pegmatite	Unaltered	Large crystals of quartz, K-feldspar and arfvedsonite	2a (minor 1)	■	■
SL-11-14	Drill core	Pegmatite core	Altered	Massive quartz and fluorite, pseudomorphs after elpidite and narsarsukite	4 and 5	■	-
SL-11-22	Drill core	Pegmatite core	Altered	Massive quartz and fluorite, pseudomorphs after elpidite and narsarsukite	4 and 5	■	-
SL-11-43	Drill core	Pegmatite core	Altered	Massive quartz and fluorite, pseudomorphs after elpidite and narsarsukite	3	■	-
SL-11-45	Drill core	Pegmatite core	Altered	Massive quartz and fluorite, pseudomorphs after elpidite and narsarsukite	3 and 4	■	-
204739	Outcrop	Subsolvus granite	Altered	Microcline, albite, quartz, arfvedsonite partially altered to aegirine, numerous pseudomorphs after elpidite and narsarsukite, associated with pore space	5	■	■
204741	Outcrop	Subsolvus granite	Altered	Microcline, albite, quartz, arfvedsonite partially altered to aegirine, numerous pseudomorphs after elpidite and narsarsukite, associated with pore space	5	■	-
204794	Outcrop	Hypersolvus granite	Altered	Perthite, quartz, arfvedsonite partially altered to astrophyllite, fluorite	2b	■	-
10205	Outcrop	Hypersolvus granite	Weakly altered	Perthite, quartz, arfvedsonite partially altered to astrophyllite	-	-	■
204762	Outcrop	Subsolvus granite	Unaltered	Microcline, albite, quartz, fresh arfvedsonite	-	-	■

Table 2 Types of inclusions

Inclusion group	Samples	Inclusion Types							Distribution
		I  Minerals	II  Gas composition/ T <sub>h</sub> (mean, °C)	III  Composition	IV  Salinity, wt.% NaCl eq./ T <sub>h</sub> , °C	V  Gas composition/ salinity, wt.% NaCl eq.	VI-1  Mineral/ Gas composition	VI-2  Gas composition	
1	204722 16 4	Fsp, Arf, Ast, Na- Zr-sil, Vil			25±5/110±70	CH <sub>4</sub> +H <sub>2</sub> /nd	Halite/H <sub>2</sub> O		
2	a 16 b 13 204794		CH <sub>4</sub> +H <sub>2</sub> /-87±5 CH <sub>4</sub> +HHc/-79±8 Nd		23±3/114±23 13.2±1.4/147±66 16.1±0.3/221±6	CH <sub>4</sub> +H <sub>2</sub> /nd CH <sub>4</sub> +HHc/16.6 <sup>1</sup> CH <sub>4</sub> +H <sub>2</sub> /nd			
3	11  SL-11-43 SL-11-45  2			Empty, traces CO <sub>2</sub> , CH <sub>4</sub>	10±4/78±10  9±5/nd 11/nd  nd	CO <sub>2</sub> +CH <sub>4</sub> /4.4±0.1  CO <sub>2</sub> /4.6±0.1 CO <sub>2</sub> /4.7±0.1  CO <sub>2</sub> /4.2±0.1	Nahcolite/ CH <sub>4</sub>	CH <sub>4</sub> ± minor H <sub>2</sub> /HHc  CH <sub>4</sub> ± minor H <sub>2</sub> /HHc	
4	7  SL-11-14 SL-11-22 SL-11-45				13.1±6.5/146±30 4±5/nd 4±4/nd 9±4/nd				
5	a SL-11-22 204741 SL-11-14 b 204739  c 7 13 SL-11-45 SL-11-22				19.2/nd 17.5/nd 17.0/nd 19.5/103±16  24±3/71±17 18.4±1.6/125±17 27±12/109±7 19±10/87±13			Zc, Tt, Fl   Ab, Mc	

<sup>1</sup> – Salinity determined by freezing point depression

Temperatures and salinities are reported as the mean ± standard deviation. HHc – Hydrocarbons with more than one carbon atom; nd – no data; Arf - arfvedsonite, Fsp – feldspar, Ast – astrophyllite, Na-Zr-sil – Na-zirconosilicates, Vil – villiaumite, Zc - zircon, Tt – titanite, Ab – albite, Mc - microcline.

**Table 3 Proportions of gases (mol.%) in the bulk fluid of different groups of fluid inclusion types based on mass spectrometric analyses of crushed samples.**

Groups	Sample	Group	N <sub>2</sub>	H <sub>2</sub>	CH <sub>4</sub>	CO <sub>2</sub>	C <sub>2</sub> H <sub>4</sub>	C <sub>2</sub> H <sub>6</sub>	C <sub>3</sub> H <sub>6</sub>	C <sub>3</sub> H <sub>8</sub>	C <sub>4</sub> H <sub>8</sub>	C <sub>4</sub> H <sub>10</sub>	Benzene	H <sub>2</sub> O	Total C (C <sub>2</sub> -C <sub>6</sub> )
<b>CO<sub>2</sub>-rich</b>	2	3	0.05	0	0.4	19.4	0	0.04	0	0.2	0.002	0.0006	0.0009	79.8	0.2
	11	3	0.4	0.02	2.4	12.6	0.002	0.7	0.03	0.4	0.03	0.02	0.001	83.5	1.2
<b>CH<sub>4</sub>-rich</b>	13	2b	2.4	0.01	9.5	1.6	0.01	2.8	0.4	1.8	0.2	0.1	0.001	81.1	5.3
	4	1	0.9	0.2	7.0	0.1	0.03	0.2	0.02	0.07	0.007	0.004	0.0001	91.4	0.3
	204722	1+2a	1.3	1.0	2.4	0.2	0.002	0.03	0.001	0.005	0.0004	0.0003	0.0001	95.0	0.04
	16	2a	0.4	0.1	3.4	0.09	0.003	0.2	0.02	0.06	0.007	0.003	0.0003	95.8	0.3
<b>Aqueous-rich</b>	204739	5	1.6	0.2	0.2	0.5	0	0.007	0.002	0.005	0.0006	0.0002	0.00006	97.5	0.015
	7	4+5	0.09	0.04	0.03	0.1	0.001	0.003	0.001	0.002	0.0004	0.0002	0.0006	99.7	0.008
<b>Hypersolvus granite</b>	10205	nd	0.4	0.02	0.05	0.5	0.00001	0.004	0.001	0.004	0.0004	0.0002	0.0002	99.1	0.01
<b>Subsolvus granite</b>	204762	nd	0.2	0.4	0.25	0.6	0.001	0.003	0.001	0.002	0.0002	0.0001	0.00004	98.5	0.007

nd – no data

**Table 4 Properties of selected fluid inclusions used to calculate isochores**

<b>Isochores (Figure 12)</b>	<b>Inclusion Group</b>	<b>Salinity, NaCl wt.% eq.</b>	<b>Th, °C</b>	<b>Partial Th, °C</b>	<b>Mol.% CH<sub>4</sub></b>	<b>Mol.% H<sub>2</sub></b>	<b>Mol.% C<sub>2</sub>H<sub>6</sub></b>	<b>Mol.% CO<sub>2</sub></b>	<b>Density, (g/cc)</b>
a	2a Aq	23	340						0.90
b	2a CH <sub>4</sub>			-85	97	3			0.21
c	2b Aq	14	284						0.88
d	2b CH <sub>4</sub>			-78	77		23		0.34
e	3 CO <sub>2</sub>		25					100	0.71
f	4 Aq	4	160						0.94
g	5 Aq	19	110						1.09

**Table 5** Calculated equilibrium proportions of gases (mol.%) as a function of temperature and oxygen fugacity. The pressure was assumed to be 1100 bar.

<b>T °C</b>	<b>H<sub>2</sub>O</b>	<b>CH<sub>4</sub></b>	<b>H<sub>2</sub></b>	<b>CO<sub>2</sub></b>	<b>CO</b>	<b>C<sub>2</sub>H<sub>6</sub></b>	<b>C<sub>3</sub>H<sub>8</sub></b>	<b>Total C<sub>2</sub>+C<sub>3</sub></b>	<b>log <i>f</i>O<sub>2</sub></b>	<b>log units below QFM buffer</b>	<b>Point N in Fig. 13</b>
500	0.4	83	16.7	0	0	0.01	0	0.01	-31.0	-7.3	1
425	0.2	96.8	3	0	0	0.02	0	0.02	-33.5	-6.2	2a
360	0.01	95.5	0.01	2.1	0.07	2.1	0.2	2.3	-34.7	-2.8	2b
350	0.01	91.4	0	5.7	0	2.4	0.3	2.7	-35.0	-3.1	-
325	0.01	48	0	45.7	0.6	4.1	1.7	5.9	-36.4	-2.7	-
300	0.01	16	0	83.4	0.1	0.1	0	0.1	-36.9	-1.2	3
225	0.01	0	0	99.99	0	0	0	0	-40.0	2.8	4

Background dataset for online publication only

[Click here to download Background dataset for online publication only: Appendices\\_FI evolution.docx](#)